Doctoral Thesis

博士論文

Optical spin-charge interconversion at non-magnetic metal/oxide interfaces
(非磁性金属/酸化物界面における光学的スピン電荷相互変換)

オブレ　フロラン

Abstract

Spintronics is based on two physical degrees of freedom: spins and charges of electrons or holes. The field of spintronics was born in 1988 with the discovery of the giant magneto-resistance by Albert Fert and Peter Grunberg, who were awarded by the Nobel prize of physics in 2007. Since then, researchers used this discovery to make significant improvements in data storage. These advancements led to the development of a new era of magnetic drives. Recently, spin conversion, a generic term for all conversion phenomena based on the principle of angular momentum conversion, is rising big interests in the electronic industry due to its possibility to lead to the development of new experimental methods as well as the implementation of novel spin conversion mechanisms. The further development of spin-conversion functionalities relies on the microscopic understanding of the interaction among quasiparticles such as electrons, spins, magnons, phonons, and photons. Recently, new types of spin-charge interconversion in non-magnetic metal/Bi_2O_3 interfaces were experimentally demonstrated where Rashba spin orbit coupling are presented. This Rashba-type spin-orbit interaction leads to the generation of magnetization from an applied electric field (direct Edelstein effect) and an electric current from a magnetic field or the magnetization (inverse Edelstein effect). This effect has some similarities to spin Hall effect and inverse spin Hall effect that also induce some spin-charge interconversion also due to spin-orbit interaction. Especially, in semiconductor/metal systems such as GaAs/Pt, it has been shown that by injecting circularly polarized light coupled with electron spins in semiconductors and it produces some transverse current through inverse spin Hall effect. Similarly, one can wonder if interactions between polarized light and Rashba-type metal/oxide system are possible as well. Relatively few studies have been done related to the interaction electron and polarized light in the presence of spatial inversion asymmetry.

In this work, we focus on investigating responses of chirality and polarization to expand the functionality of the spintronics devices. First, we investigate the creation of spin accumulation at the interface of metal/oxide system by direct Edelstein effect. By injecting AC charge current and a magneto-optical Kerr effect system, we detect spin accumulation and give a proof of that Cu(Ag)/Bi_2O_3 have a strong Rashba effect at the interface. Then, we investigate the possibility of the creation of charge current by injection of polarized light on Cu/Bi_2O_3 interface by inverse Edelstein effect. Above the band gap of Bi_2O_3, spin to charge conversion is expected, similar to Pt/GaAs interface. But more surprisingly, we also observe spin to charge conversion below the band gap of Bi_2O_3.

Spin accumulation induced by spin Hall effect was first directly observed when passing non-polarized electrical current in bulk GaAs and strained InGaAs by using a magneto-optical Kerr effect system. The detected spin polarization was found to be opposite at opposite edge of the samples. Analogously to spin Hall effect, direct Edelstein effect is a physical phenomenon that permits the generation of non-equilibrium spin polarization from electrical charge current, which in turn leads to the build-up of spin accumulation.

We show the observation of the spin accumulation in non-magnetic metal/bismuth oxide interface by using time-resolved transverse magneto-optical Kerr effect (TR-TMOKE) at a laser wavelength of 408 nm. Generally, TMOKE should result in a change in intensity rather than a change in Kerr rotation, when working with pure p-polarized light. However, in our TR-TMOKE setup, signal significantly enhanced by utilizing mixture of s- and p-polarized light. We apply modulated AC voltage along the interface, which aligns spins perpendicularly to the electrical charge flow. We show that TR-TMOKE signals for Cu/Bi_2O_3 and Ag/Bi_2O_3 interfaces coincide with the excitation AC sinusoidal voltage. Correlation between the AC excitation voltage and the TR-TMOKE signal directly assures the presence of spin accumulation induced by direct Edelstein effect in our devices. More interestingly, the MOKE signals from these two interfaces show opposite phases, indicating opposite spin-momentum locking configuration. This opposite spin-momentum locking has also been confirmed by spin pumping experiments in the same interfaces done by our group. We also describe the relation between the amplitude of our TR-TMOKE signals and the expected spin accumulation. The amplitudes of Cu/Bi_2O_3 and Ag/Bi_2O_3 signals are giving a ratio of 1.45 and are in good agreement with the ratio of their estimated spin accumulation equal to 1.69. Also, we explain the difference of the optical detections of spin accumulation generated by spin Hall effect and Edelstein effect. Intrinsically, spin accumulation generated by bulk spin Hall effect and direct Edelstein effect at interfaces have a different distribution of spin orientations. Spin polarization via bulk spin Hall effect is oriented perpendicular to the charge current on all the four planes which are transverse to the charge current. In contrast, spin accumulation via Edelstein effect is in-plane at interfaces, homogeneous and perpendicular to the charge current direction. In the experiments, the spin accumulation is generated at the Cu/Bi_2O_3 and Ag/Bi_2O_3 interfaces, and it is possible for these spins to diffuse into the metal. If the spin diffusion length is larger than the thickness of nonmagnetic metal layers, the quantity of detected spin accumulation is increased with the penetration depth of the laser. We evaluate a possible enhancement of the signal by a factor of 9.3 in our sample. In the end, we show for the first time detection of spin accumulation at the interface of non-magnetic metal/oxide and give an estimation of the detected spin accumulation by our system of 130.2 μeV for Cu/ Bi_2O_3 and 220.4 μeV for Ag/ Bi_2O_3.

Moving on, we show the possibility of the creation of charge current by circularly using the same devices. We start with a measurement of the optical absorption of our Cu/ Bi_2O_3 device by UV-Vis-NIR absorption spectroscopy, in the range from 0.9 eV to 6.2 eV. We find out that the absorption spectra displays two interesting optical transitions,

one at 3.13 eV and the other at 2.12 eV. The optical transition at 3.13eV corresponds to the band gap of Bi_2O_3 and the transition around 2.12 eV corresponds to the plasmonic absorption of copper. To characterize deeply these two optical transitions, we use continuous wave laser at different energies (1.15 eV, 1.96 eV, 3.05 eV). We vary the incidence angle θ, and the photon polarization by using a linear polarizer and a quarter wave plate mounted on a mechanical rotator. The photovoltage is detected perpendicularly to the incidence beam by a lock-in amplifier synced with a mechanical chopper. We show that light-polarization information can be converted into an electric signal by combining the optical selection rules and the inverse Edelstein effect. By using a laser with a power of 1mW and an energy of 3.05 eV, which is close to the band gap of Bi_2O_3, we measure the incidence angle dependence of the detected circular photovoltage and it shows a maximum value at an incidence angle θ = 50° with a value of 3.1 μV. We explain this result by analogy of previous experiments in Pt/GaAs that shows inverse spin Hall effect. Indeed, in a semiconductor, the optical selection rules for interband transitions induce spin-polarized electrons in the conduction band via the absorption of circularly polarized light. This process transfers light circular polarization into electron-spin polarization. Then, depending on the spin momentum locking at the interface, the spin polarized electron diffuses transversally in a direction.

We also measure the circular photovoltage depending on the incidence angle dependence by using a laser at 1.96 eV energy. More surprisingly, it shows that this dependence of photovoltage is different from the behavior at 3.05 eV energy. The voltage behavior created by the circularly polarized light for a laser power of 1.5 mW looks linear and can reach 15 μV which is five times bigger than at 3.05 eV. Using the previous scenario, it would be expected that no circular photovoltage could be detected because the energy of the laser is below the band gap of Bi_2O_3. One hypothesis is to attribute this circular photovoltage to plasmonic like absorption of the heterostructure. Photovoltaic devices based on plasmon induced hot electrons at metal/oxide nanoparticles have shown large conversion efficiencies. We compare this circular photovoltage with the response of a Cu(111) layer to a circularly polarized light at 1.96 eV, where the optical absorption of plasmon surface states is expected. However, we do not observe significant transverse voltage related to circularly polarized light. Also, we measure the sample with a laser at 1.15 eV energy. Neither do we observe transverse voltage. This suggests that a combination of plasmon-induced hot electrons and inverse Edelstein effect as the origin of our polarised photovoltage is at the Cu/Bi_2O_3 interface.

One hypothesis to explain the difference of oblique incidence dependences at 1.96 eV and 3.05 eV can be that two main factors are contributing to the signal: the degree of circular polarisation and the angle dependence between spin polarization vector (σ_s) and the spin current (J_s) such as $V_c \propto \sigma_s \times J_s$. Above the band gap, the degree of circular polarization depends on the absorption coefficients for s-polarised component and p-polarised component, which are unaffected at normal incidence (θ =0°) and decrease significantly at higher angles. Js is negligible at normal incidence (θ =0°) and gradually increases towards the maximum at grazing angles. As a result, for an excitation energy

above the Bi_2O_3 band gap, a minimum of V_C is located at θ=0° and a maximum is at θ=50°. However, below the band gap of Bi_2O_3, the photons are not absorbed in the Bi_2O_3. Meanwhile, their degree of circular polarization is negligibly affected by the incidence angle, just only showing that oblique incidence dependence on $\sigma_s \times J_s$, possibly explaining the linear dependence.

To summarize, we studied the effects of optical spin-charge interconversion at the non-magnetic metal/oxide interfaces. Especially, we are able to characterize the spin accumulation at Cu/Bi_2O_3 and Ag/Bi_2O_3 interfaces and show that these interfaces have opposite spin momentum configuration. Also, we illustrate that circularly polarized light with an energy near the band gap of Bi_2O_3 can be converted into charge current in Cu/Bi_2O_3 interface. More surprisingly, we reveal the existence of helicity dependent photovoltage at energy range close to the plasmon resonance of copper. Also, the result from optical spectroscopy shows plasmonic like absorption at Cu/Bi_2O_3 interface. Based on these results, we hypothesize a new mechanism for photovoltage generation that relies on plasmon resonance and Rashba interfaces. To sum up, we demonstrate that plasmonic energy conversion holds the promise for efficient mechanism of electron-hole separation in photovoltaic devices at low costs. Moreover, the study reflects the relevance of selecting appropriate engineering of heterojunctions. Furthermore, considering the increasing interest of systems with spatial inversion asymmetry, we expect that the presented work would motivate further studies on advancing conversion efficiencies and further understanding towards spintronics in photovoltaics.

DEDICATION AND ACKNOWLEDGEMENTS

As a thesis is not a work of only one person, I would like now to thank all the people I collaborated and there are a lot. I would really like to thank RIKEN and ISSP people that contributes to create its great environment, founded on team work and good humour, that makes the work here a real pleasure.
At first, I would like to thank my advisor professor **Yoshichika Otani** for giving me the opportunity to pursue PhD in his group. Since I arrived in 2013 as an internship student to now, he helped me to grow up by giving me constant thoughtful suggestions and continuous support. He gave me many oppotunities to present my research results in domestic and international conferences.
I thank also very grateful to the reviewers of my thesis **Shik Shin**, **Iwao Matsuda**, **Noriaki Kida** and **Naoki Ogawa** for accepting to be the reviewers of my thesis and giving me very helpful advices and comments on my manuscript.

Also, I deeply thank **Jorge Luis Puebla Nunez** who I have been the honor to work with. With his undefeatable optimism, he helped me, believed in me and in my results. I also appreciate his kind help to me when I am in trouble. During my PhD, he taught how to do research, how to write abstracts of conferences and manuscripts for journals, how to make presentations and of course, how to carry out research and how to use equipments. And I would like to thank him more than I can write here.
I would like to especially thank my dear colleague **Mingran Xu** for all the time we spend together, working and chatting about the world. I am sure his PhD and career after will be very successful.
Also, I would like to thank **Yasuhiro Niimi**, thanks to him and all his help all through my three months internship in the lab back to 2013, I was able to to get a scholarship to study in Japan. In the same way, I would like to thank my very first colleague **Yasutomo Omori**. Five years ago, we worked together on ISHE in loop shape and it has been the start of my studies in the spintronics field.

Not only did I have the chance to travel Europe extensively during this three-year, but I even got the opportunity to spend two months in Germany. For this invaluable and unforgettable experience, I would like to express my deepest gratitude to professor **Sergey Ganichev** from the University of Regensburg. I had a wonderful experience in his laboratory and especially a big thank you to **Sergey Danilov** and **Maximilian Otteneder** for the help their provided me even though the results were not as successful

as I expected. I wish you continuous achievements both in personal life and academic life.
I also want to thank professor **Mikk Lipmaa** who helped me to carry out growth of ZnO using PLD. I learnt some depositions methods I had never seen before thanks to you.
As support is always needed when making and characterizing samples, I would like to thank all the people working in clean room in RIKEN and especially **Kazuhiko Shihoyama** and **Satoshi Amaya** who were always here to help me when I was in trouble with some machines. In the same way, I also want to thank **Daisuke Hashizume** who was always kind and give helpful advices on the samples characterizations in RIKEN. And also **Satria Zulkarnaen Bisri** for helping me characterizing my samples using optical spectroscopy.

There are also all the present and former members of Otani group that makes the atmosphere here a pleasure. So a deep thank to people in RIKEN where I spent most of my PhD. I would like to thank all the post-docs and researchers **Kouta Kondo**, mister **Bivas Rana**, **Junyeon Kim**, **Tomoyuki Yokouchi** and **Yasuhiro Fukuma** for giving me advices on my ideas and listen way too many times my rehearsals for presentations. Also, the past and present students **Shutarou Karube**, **Norinobu Hasegawa**, **Tsai Hanshen** and **Heeman Kim** for laughing with me, accept me and checking my crazy ideas. And also, I would like to acknowledge all the the internship students that came to visit us **Xavier Simon**, **Vincent Berdeu**, **Edurne Sagasta**, **Jamie Massey**, **Eva Kempf**, **Samiran Choudhury** and **Jiang Nan**. Among them, I would like to especially thank **Antoine Albouy** with whom I had a extensive pleasure time in clean room and who produced a fantastic work during his stay. I wish you all the best for the future. To conclude about Riken, I would like to deeply thank **Machie Kaito** for all the help and laugh in clean room and the very person who helps everyone in the shadow and makes this laboratory be so efficient **Michiko Ishinabe**. As for ISSP, I would like to thank **Motoi Kimata**, **Hironari Isshiki**, **Prasanta Kumar Muduli**, **Satoshi Sugimoto**, **Taro Wakamura**, **Tomoya Higo** and **Naemi Riccarda Leo** for your kindness and all the knowledge you shared with me. And all the present and past students I shared some time with : **Sei Takizawa**, **Hideki Narita**, **Kenta Matsumoto**, **Yusuke Uchida**, **Nobuto Kurihara**, **Yuki Mogi**, **Ayuko Kobayashi**, **Zheng Zhu**, **Shinji Nakada**, **Mingxing Wu**. I wish you good luck and extensive pleasure in your studies and hope a bright future for all of you. And lastly, a big thank to **Junko Kawamura**, **Chiemi Ota** and **Yoko Kaneda**, the department of material sciences and the graduate school of frontier sciences for all the administrative help.

Even if my PhD was taking a lot of my time, I still had some to see and make some friends in Japan. I would like to especially thank my friends who supported me all through this though process. At first, I would like to thank **Amaury Josse** who has always been here since I am in Japan and helped through the hard time of my thesis with his unconditional support and help. I want to thank **Alban Lafuente-Sampietro**, **Jill-Jenn Vie** and **Zoe Schellenbaum** for coming to my defense, it was a pleasant surprise to see you and I hope you could understand something. Also, a big thank

to **Raphael Gaschignard** and **Vincent Tran** with whom I have endless discussion with since 2014 and also all my friends : **Nana Arizumi**, **Cédric Bareille**, **Jeanne Becdelievre**, **Laura Catella**, **Florian Castelanne**, **Haroun Chin**, **Cao Tri Do**, **Florent Dinet**, **Lucile Fournereau**, **Aven Guan**, **Johan Hamonnet**, **Hana Hirose**, **Christopher Kirhkam**, **Ian Lamaignere Sheri Lin**, **Philippe Mathieu**, **Ammar Mian**, **Ines Michel Marie-Charlotte Savary**, **Son Tran Quang**, **Tomooki Shiba**, **Edouard Pavageau**, **Vincent Philippe**, **Damir Pinek**, **Avril Treille** and **Arthur Rosset**. Don't be offended if I forgot your name, I have a bad memory...

At the end I would like to thank my familly. My parents **Marc Auvray** and **Xuan-Lan Auvray** for the financial and emotional supports, my dear grand-mother **Louise Auvray** and my uncles **Eric Auvray** and **Christophe Auvray**.

Finally, I appreciate financial supports by the Ministry of Education, Culture, Sports, Science and Technology - Japan and the University of Tokyo.

TABLE OF CONTENTS

List of Tables

Table **Page**

List of Figures

Figure **Page**

CHAPTER 1

INTRODUCTION

1.1 Retrospective of Spintronics

We start with a brief summary of Spintronics. Spintronics is based on two physical degrees of freedom: spins and charges of electrons or holes. The field of Spintronics was born in 1988 with the discovery of the giant magneto-resistance by Albert Fert [1] and Peter Grünberg [2], who were awarded by the Nobel prize of physics in 2007. The effect observed was a change in the electrical resistance of a trilayer thin film composed of a nonmagnetic layer of chromium sandwiched by two ferromagnetic layers of iron. The scattering of spin-polarized electrons depends on the magnetization direction of the ferromagnetic layers, which can be parallel or anti-parallel, inducing magnetic resistance. By using an external magnetic field to change the direction of magnetization of the layers, they found out a change of 20% of the electrical resistance at room temperature and up to 85% at 4.2K. Since then, researchers used this discovery to make significant improvements in data storage. These advancements led to the development of a new era of magnetic drives, a technology recognized in 2014 with the Millennium Technology Prize, received by Prof. Stuart Parkin [3]. Recently, spin conversion, a generic term for all conversion phenomena based on the principle of angular momentum conversion is rising big interests in the electronic industry [4, 5] due to its possibility to lead to the development of new experimental methods as well as the implementation of novel spin conversion mechanisms. So far, the most famous phenomenon is the spin Hall effect (SHE) that converts charge flow into a transverse spin current which is a flow of angular

momentum without charge flow.

Spin Hall Effect

Spin Hall effect has been first observed optically by Kato et al. in 2004 [6]. In this experiment, generation of spin accumulation was done in GaAs/InGaAs heterostructures by injecting unpolarized charge current and detecting the resultant spin accumulation using a spatially resolved magneto-optical Kerr effect setup (MOKE).
It is also important to notice that this effect has an opposite effect called inverse spin Hall effect (ISHE), which is the conversion of spin current into charge current. Following the optical observation of SHE, several electrical detections of SHE and ISHE have been made. The first observation of ISHE was made in 2006 by Saitoh et al. [7] using a bilayer of permalloy (Py), a ferromagnetic material, and Platinum (Pt) which is a material with strong orbit interaction. This group used spin pumping technique which consists of injecting high-frequency microwave that creates a spin current from Py that diffuses into Pt, which converts it into detectable voltage. The theory of spin pumping has been first theorized in 2002 by Y. Tserkovnyak et al. [8, 9]. However, in this experiment, relevant parameters related to the effect could not be extracted from the detected signal. Following this experiment, Otani group in 2007 [10] experimentally detected SHE and ISHE at 77K and, more importantly, at room temperature. Electrical detection of the spin and charge accumulations via direct and inverse SHEs were done using Py/Cu/Pt non-lateral spin valve structures. This technique enables to detect the spin-Hall signal generated over the spin diffusion length of a few hundred nanometers, and allows the quantification of numerous quantities, such as the spin Hall conductivity and the spin to charge conversion called the spin Hall angle which was 0.37% for Pt, the largest value reported at the time. Since then, this technique has been exploited to characterize many materials such as 4d/5d transitions metal [11], diluted alloys [12, 13], Graphene/Pt [14] and topological insulators [15]. Besides this electrical characterization, it has been shown similarly that light-polarization information can be converted into an electric signal by combining the optical selection rules using GaAs/Pt bilayer [16] and ISHE.

Photoinduced current using inverse spin Hall effect

Circularly polarized light can also be coupled with electron spins in semiconductors. In 2010, Ando and al. [16] showed that in a semiconductor/metal systems such as GaAs/Pt. When polarized light is shined on the system, the angular momentum of the light is

transferred to the semiconductor, inducing spin-polarized carriers through the optical selection rules for interband transitions. Then, this spin-polarized current is transferred into the Pt layer and converted into a transverse current by inverse spin Hall effect. This effect has been shown since then in many similar systems, such as InP/Au [17], Ge/Pt [18] and more recently Si/Pt [19].

Edelstein effect

In recent years, studies of two-dimensional systems related to spintronics have been more and more explored. It first started with Datta and Das [20] that proposed a type of transistor using spin-polarized field effect and two-dimensional electron gas, which was later realized by Nitta et al. [21] in $In_{0.53}Ga_{0.47}As/In_{0.52}Al_{0.48}$ heterostructures. These systems rely on the Rashba spin-orbit coupling. A Rashba system is a two-dimensional condensed matter system that has a momentum-dependent splitting of spin sub-bands. Due to the spin polarization of the surface and bulk states, the application of an external electric field is expected to induce a macroscopic spin polarization at a two-dimensional condensed matter system. In systems with broken inversion symmetry and spin-polarized surface states, such as Rashba and Dresselhaus systems, this phenomenon is known as the Edelstein effect. But up to now, all the systems that have been measured were based on semiconductors materials [22]. However, recently this phenomena emerged in other types of structures such as metal/metal interface in Ag/Bi [23] and topological insulator using α-Sn [24], both done by Rojas-Sanchez et al. and using the spin-pumping technique to characterize them. Similar to ISHE, the creation of charge current from the spin current at the interface is called the inverse Edelstein effect. Applied research so far has focused on SHE which is spin current conversion to induce magnetization reversal switching. However, these physical properties are inherent to the spin-orbit interaction of the bulk of the material. On the other hand, in Rashba interfaces, it is possible to form different interfaces tuning the properties depending on a panel of an infinite set of combinations.

1.2 Motivation

From all these studies presented before, we can understand how important spin current is in spintronics area. In order to boost spintronics researches and devices applications, a broad understanding of transport properties of spin current is required. Especially, the

generation and detection of spin current is indispensable not only for device application but also for characterizing the transport properties of spin current. Previous reports showed that the generation and detection of spin current and spin accumulation were possible using materials displaying strong bulk spin-orbit interaction. However, the interest is also shifting into low-dimensional systems such as Rashba interface because they possess advantages such as tunability of spin interaction [5]. However, few reports are using these newly available properties, especially using light to characterize these interfaces. A previous report from Karube et al. [25] showed enhanced spin relaxation took place at the Ag/Bi_2O_3 interface in the spin transport measurement, and a possible scenario was that the relaxation process was affected by Rashba spin-orbit interaction at the interface. Bi_2O_3 shows some high refractive index and dielectric permittivity, as well as marked photoconductivity and photoluminescence [26]. It makes non-magnetic metal and Bi_2O_3 interface and bulk light-matter interactions interesting to study. Also, symmetry analysis can provide a valuable understanding of systems, particularly because it reveals which quantities are conserved and which ones can be transformed. In this context, helicity can be a useful addition to more commonly considered observables. So here, our motivation is to unveil the entanglement between polarized light in an interface made of non-magnetic metal and oxide displaying strong spin-orbit interaction and strong light-matter interaction such as Bi_2O_3.

1.3 Outline

This thesis consists of 5 chapters. Chapter 1 describes the general introduction and the motivation of this thesis. Chapter 2 summarizes the theory on metal/semiconductor interfaces, spin-orbit interaction, Edelstein effect, Magneto-Optical Kerr effect and polarization dependence. Chapter 3 describes the detection of spin accumulation of non-magnetic metal/oxide interface by using the magneto-optical Kerr effect system. We found out that a very low Kerr ellipticity could be detected if the system is tuned correctly and that the sign of the Rashba parameter could be detected. Chapter 4 describes the interplay between non-magnetic metal/oxide systems and polarized light. Surprising behaviors appeared. When excited with some light energy above the band gap of the oxide, a voltage can be detected, very similar to photoinduced current using ISHE in GaAs/Pt [16] presented before. However, when we excite below the band gap, some even bigger voltage is detected. We assume a novel mechanism using surface states plasmon resonance and Rashba interface made by non-magnetic metal/oxide. The last chapter

summarizes the study and gives perspectives.

CHAPTER 2

THEORY

This chapter aims to present the main theoretical tools one needs to understand to this thesis. As we study the interconversion between polarized light and metal/oxide interface that is showing some 2D electron gas feature, we will outline in this chapter, the principle of spin-orbit interaction and its relation with Rashba effect and the Edelstein effect.

2.1 Metal/Semiconductor contacts

2.1.1 Introduction

Semiconductors have some interesting properties that make their conductivity tunable by external factors such as electric current, magnetic fields or light. But, application of semiconductors in electronic devices needs electrical contacts which are metallic. So, metal-semiconductor interface understanding is an essential tool to use semiconductors. Braun in the 19^{th} century[27] created the first semiconductor device which was a rectifying metal-semiconductor interface. But, he was attributing the behavior to an extreme high resistive thin surface layer at the interface [27]. Later on, Schottky attributed this rectifying behavior at the metal-semiconductor interface to the presence of a potential barrier, giving a depleting layer on the semiconductor side of the junction. He proposed model to predict the barrier by using the difference between electron affinity of the semiconductor and the metal work function[28].

However, some discrepancy appeared in the model compared to some experimental re-

sults. In 1947, Bardeen showed that a high density of states at the interface from surface states of metal-induced gap states lead to a Fermi level pinning which can cause this discrepancy.

In this section, we show the basics of metal-semiconductor contacts and Schottky-Mott rules, the concept of metal-induced gap states and surface photovoltage effect that will be essential for the correct characterization of the characteristics of the metal/semiconductor interface we will use experimentally in chapter 4 and 5.

2.1.2 Basics of metal-semiconductor contacts and Schottky-Mott rules

The rectifying behavior of the metal/semiconductor junction was described as it was generated by space-charge region on the semiconductor edge of the interface. Here, the semiconductor does not have any surface states within the band gap, and the bands are flat. The energy-band diagram of a metal/semiconductor junction is schematically represented in figure 2.1. The work function of the metal Φ_M and semiconductor Φ_S are the energy difference between their Fermi level and the vacuum level. The electron affinity of semiconductor χ is the energy difference of its conduction band edge and vacuum level. According to the Schottky model, when a metal and semiconductor with different work functions are brought into the contact, an electric field is produced as a result of their work function difference and matching of the Fermi level. This alignment of Fermi level makes the electric field enters into the semiconductor. The work function of the semiconductor increases as the electric field penetrates and accordingly, the potential lowers by V_{bi}, called built-in potential.

If we assume an abrupt contact for an ideal metal and a p-type semiconductor the Schottky barrier height can be given by [28]

$$\Phi_{Bp} = \Phi_M - \chi \tag{2.1}$$

Moreover, for a metal and p-type semiconductor it can be expressed as :

$$\Phi_{Bp} = E_g - (\Phi_M - \chi) \tag{2.2}$$

With E_g the band gap of the p-type semiconductor. As said before, V_{bi} which is the built-in potential that the electrons feel during their motion into the metal can be determined

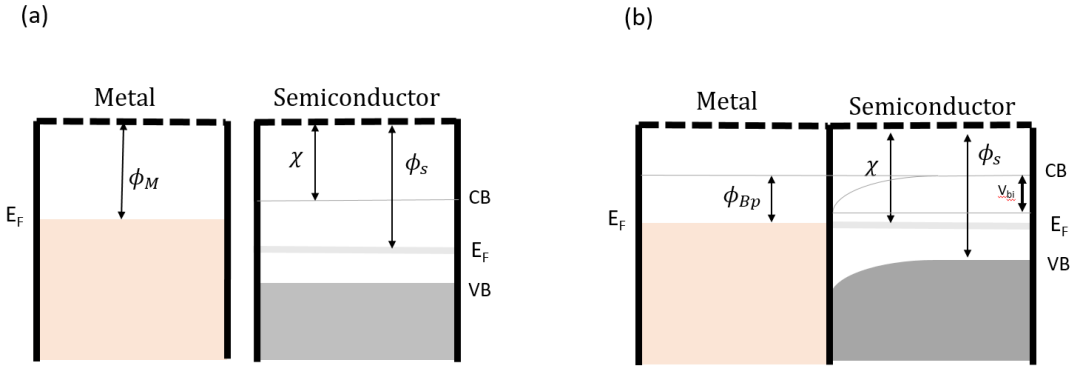

FIGURE 2.1. Energy band diagram of a metal in contact with a p-type semiconductor (a) before the contact (b) after the contact

by

$$V_{bi} = \Phi_{Bp} - V_n \tag{2.3}$$

with V_n the energy difference between the Fermi level and the conduction band.

When a semiconductor and a metal are in electric contact, a depletion layer forms at the junction as a result of the charge transfer across the interface and diffusion of the carriers away from the junction. A depletion layer is free of mobile carriers and acting as a potential barrier which prevents the flow of electrons (holes) from metal (p-type semiconductor) to the n-type semiconductor (metal). According to the Schottky-Mott rule, three types of contacts can form depending on the difference between the work function of the metal and the semiconductor. They are called accumulation, neutral and depletion, as the majority of carriers are accumulated, unchanged or depleted at the interface.

Figure 2.2 represents these three different metal p-type semiconductor interfaces [28] before the contact at the upper part and after the contact at the lower part. Accumulation and neutral contacts are ohmic, while the depletion one is Schottky. In the ohmic contact cases, the contacts have negligible resistance, and electrons can flow between the two materials. However, the experimental barrier heights are not usually consistent with the prediction of the Schottky-Mott rule as they do not usually depend on the metal work function. The reason is that this model, it does not consider the chemical reaction and the effect of the atomic structure at the interface interactions. Bardeen [29] proposed that the charged surface and interface states, which are accompanied by a double layer of charge can lead to a so called Fermi level pinning. It means that the absorption of the charges coming from the metal into the semiconductor by these states are shielding the

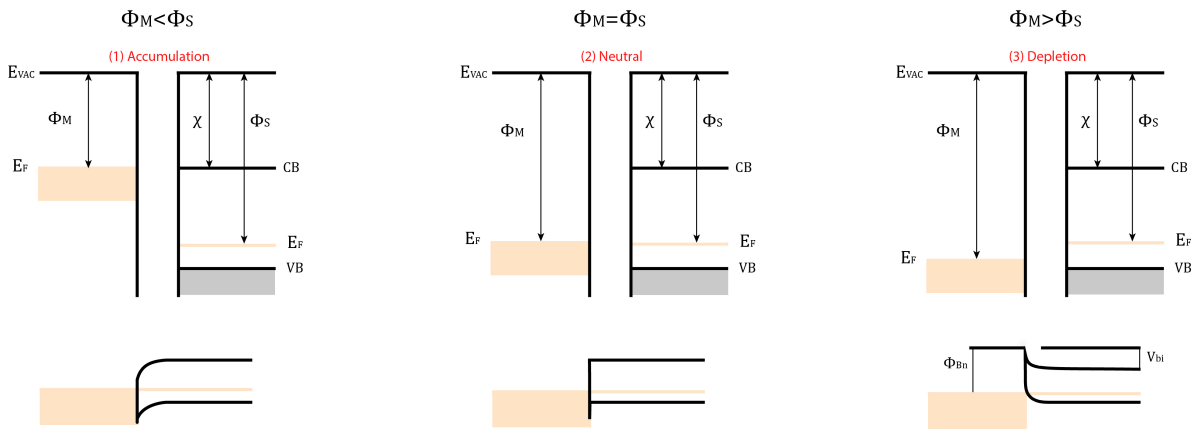

FIGURE 2.2. Schematic Representation of the band diagram of three possible metal-p-type semiconductor contacts according to the Schottky-Mott rule. Upper part displays the metal and the semiconductor energy-band diagram before the contact, and lower part shows them after the contact.

semiconductor from the details of the metal. Therefore, the bands line up concerning these charged surface and interface states [29].

In the next subsection, this phenomenon and the metal-induced gap states model will be discussed.

2.1.3 Concept of Metal-induced gap states

As mentioned in the previous section, the interface states can penetrate in the band gap of the semiconductor at Schottky junctions. As a result of the charge neutrality, the net charge in the metal side is equal to the sum of the net charge of the interface states and the space-charge region on the semiconductor side in the equilibrium. It is possible to interpret the physical origin of these states like this: In bulk crystal of a semiconductor, it is possible to assume that the potential has the periodicity of the lattice. At the edge of the semiconductor, meaning at the surface or interface states, there is a break periodicity that result in a change of the wave functions of the electrons. The periodicity deviation can be as a result of either intrinsic surface and interface states or extrinsic ones such as the bulk defect of the semiconductor [30]. At metal/semiconductors interfaces, the wave function of the electron in the metal and in the semiconductor should match. Therefore, the metal wave functions tail extends into the semiconductor because of the overlap between the metallic band and the band gap of the semiconductor, as

shown schematically in figure 2.3.

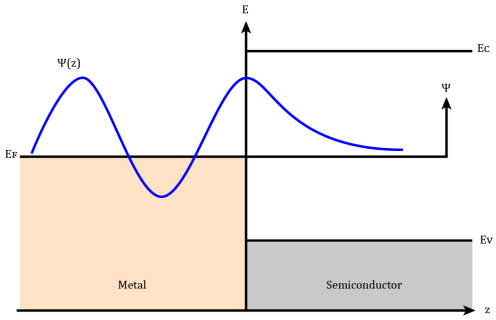

FIGURE 2.3. Representation of the metal Bloch state Ψ(z) near the Fermi level which decays into the semiconductor. Adapted from [28]

The deviation of periodicity at the contact leads to the formation of decaying interface states and results in the creation of these virtual gap states within the forbidden gap of the semiconductor. So what we are especially interested here is the metal-induced gap states that lie in the range of the energy that conduction band of the metal overlaps the band gap of the semiconductor. The wave functions of this type states are bulk-like in the metal decaying rapidly into the semiconductor.

2.1.4 Surface photovoltage effect

The surface photovoltage effect was seen and explained by Bardeen and Brattain, when they studied the photon-induced variation on Ge [31]. The effect is as following : when a semiconductor is irradiated by light, electron-hole (e-h) pairs are generated via interband transitions or releasing captured carriers through trap-to-band transitions. The photon-induced electron-hole pairs move in opposite directions as a result of the potential in the space-charge layer. The most important for our research is that a similar phenomenon happens at the Schottky metal/semiconductor contact, when it is exposed to light. If the photon beam impacts on a rectifying interface, e-h pairs will be created and followed by spatial redistribution inside the sample because of the electric field. For example, in a rectifying metal-p-type semiconductor contact, holes are forced to move towards the bulk of the semiconductor due to the presence of the potential difference whereas the electrons are trapped at the surface to compensate space-charge region as shown in figure 2.4

The surface photovoltage effect does not occur at ohmic contacts, at which the carriers flow easily, and the recombination rate is too small to allow for the charge redistribution.

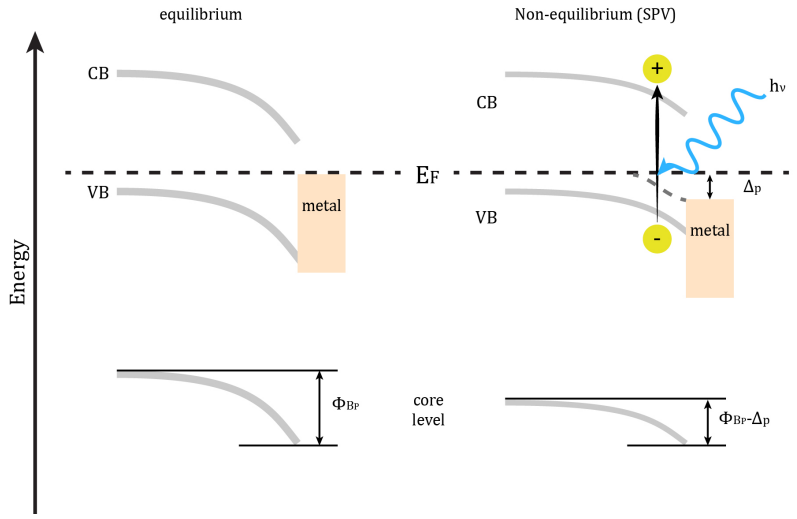

FIGURE 2.4. Schematic representation of the band alignment in equilibrium (a) and in the presence of the surface photovoltage (b), leading to the shift of the band and reduction of the barrier height at metal-p-type semiconductor interface.

An excessively thick metal layer opposes the electrons, excited at the surface of the semiconductor crystal, from penetrating through the metal layer and hinders thus the measurement of the surface photovoltage effect. As a result, the Fermi level coincides with the reference Fermi energy. The magnitude of the surface photovoltage depends on different parameters, for example, photon intensity, band bending, combination rate, defaults concentration, and temperature.

2.2 Rashba spin-orbit interaction

2.2.1 Intuitive description

Spin-orbit interaction gives a coupling between the dynamical spin of an electron and its orbital motion in space. Intuitively, if an electron is traveling through an electric field, it can see in its rest frame moving charges. Charges motion or more simply electrical current gives rise to an internal magnetic field in the rest frame of the electron. The magnitude and the direction of this internal magnetic field will depend on the velocity and the travel direction of the electrons in the material. Spin-orbit interaction gives rise to a k-dependent internal magnetic field, with k the wavevector of the electrons. We will see that spin-orbit interaction can lift the spin degeneracy which will result in a

k-dependent spin-splitting of the conduction band.

2.2.2 Spatial inversion asymmetry

In a centrosymmetric crystal, the spin-up and spin-down have same energy on the same momentum. It is called degenerated state.

Spin degeneracy is the consequence of combined time reversal

$$E(\uparrow,-\mathbf{k}) = E(\downarrow,\mathbf{k})$$

And spatial inversion symmetry

$$E(\uparrow,-\mathbf{k}) = E(\uparrow,\mathbf{k})$$

which will give :

$$E(\uparrow,\mathbf{k}) = E(\downarrow,\mathbf{k})$$

In a scenario where there is a two-dimensional electron system, the spatial inversion asymmetry (SIA) lifts the spin degeneracy.

$$E(\uparrow,\mathbf{k}) \neq E(\downarrow,\mathbf{k})$$

In general, it is described by the so called Bychkov-Rashba model [32]:

$$\hat{H}_R = \alpha_R[\mathbf{p}\times\sigma]\cdot\hat{z}$$

where $\mathbf{p} = -i\hbar\nabla$ is the momentum operator $\sigma = (\hat{\sigma}_x,\hat{\sigma}_y,\hat{\sigma}_z)$ is vector of the Pauli spin matrices and $\hat{z}$ is a unit vector which is directed in the normal to heterojunction.

The total Hamiltonian of the electrons is given by $\hat{H} = \hat{H}_0 + \hat{H}_R$ which is

$$\hat{H} = \frac{\mathbf{p}^2}{2m} + \alpha_R[\mathbf{p}\times\sigma]\cdot\hat{z} = \frac{p_x^2+p_y^2}{2m} + \alpha_R(\hat{\sigma}_x p_y - \hat{\sigma}_y p_x) \tag{2.4}$$

Solving this Hamiltonian gives the following energy spectrum :

$$\mathbf{E}_{\pm}(\mathbf{k}) = E_0 + \frac{\hbar^2 k^2}{2m_e^*} \pm |\alpha_R||k| \tag{2.5}$$

The two possible spin direction is shown by the plus or minus sign. As said previously, it follows that Rashba spin-orbit interaction leads to lifting the spin-degeneracy of the

conduction band, even in the absence of an external magnetic field. Rashba spin-orbit interaction results in a spin-splitting of $\Delta = 2\alpha_R|k|$. A presentation of the dispersion relation is shown in figure 2.5. The Rashba parameter α_R is expressed as:

$$\alpha_R = (\frac{2}{c^2}) \int \frac{\partial V}{\partial z} \psi^2 dz \tag{2.6}$$

With c is the speed of light, $\partial V/\partial z$ is the potential gradient, ψ^2 is electron density distribution. From that, most important information of the splitting are summarized in Rashba parameter. The energy of Rashba spin-orbit interaction and the splitting direction reflects the amplitude and sign of the Rashba parameter.

As said in the introduction, Rashba-Bychkov model has been successfully applied to surface state and interface state of metallic systems. However, the origin of these giant Rashba type splitting is still under debate. The most accepted concept claims that the indispensable contribution from strong spin-orbit interaction, spatial inversion asymmetry and structural parameters [33, 34]. Despite hot debates, manipulating spin in Rashba systems has been intensively studied. In the following chapters, we will show a practical examples usage based on Edelstein effect and inverse Edelstein effect is introduced.

2.2.3 Edelstein effect

It was predicted by Edelstein in 1989 [35] that the absence of "up-down" symmetry in two-dimensional electron systems permits a magneto-electric effect. As mentioned in the previous section, the spatial inversion asymmetry induces an additional spin-orbit interaction term, allowing a resultant magnetic field as shown in figure 2.5). Although, in equilibrium state, the average built-in magnetic field equals to zero, when applying an electric current, the drifted electron distribution gives a non-zero magnetic field as shown in figure 2.5. This non-zero magnetic field is normally termed as spin accumulation which represents an unbalanced chemical potential of the spin state. This phenomenon is generally depicted as a shift of Fermi contour as shown in figure 2.5 (a). The reciprocal effect, called inverse Edelstein effect describes a scenario where the injection of spin state induces an out of equilibrium state, resulting in an electric potential in the plane of two-dimensional electron gas as shown in figure 2.5 (b).

From 2013, Rojas Sánchez and colleagues experimentally demonstrated the spin to charge conversion in a Rashba interface [23, 24] in metal/metal interfaces. However, this

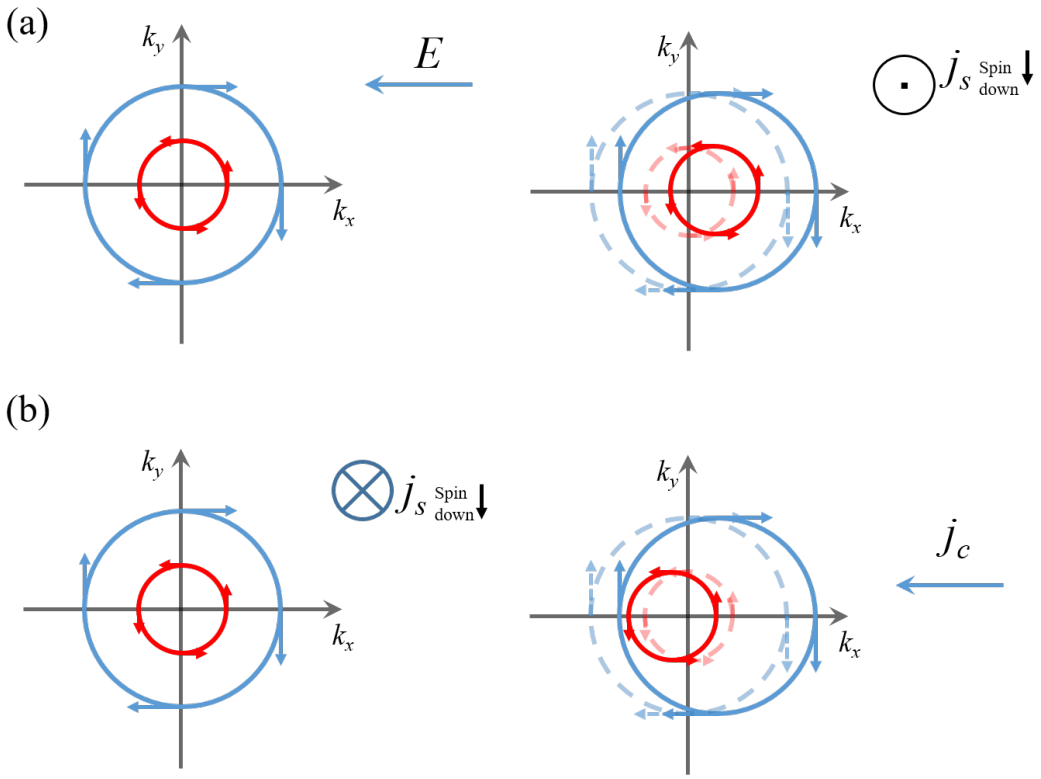

Figure 2.5: Schematics of direct Edelstein effect (a), and inverse Edelstein effect (b).

observation of relevant phenomenon asks for extremely high-quality films, in order to have to have a well-defined interface structure. However, a recent report from Karube [36] shows large conversion efficiency in an amorphous semiconductor (Bi_2O_3) and copper interface. This unexpected result easy the path of obtaining materials presenting Rashba type interaction in metal-semiconductors interfaces.

2.3 Surface plasmons resonance

2.3.1 Introduction

Even if it was more than a century ago, when the anomalous dark bands observed in the spectrum of light reflected from a metallic diffraction grating were first reported by Woods in 1902 [37]. Then in 1941, Fano linked this phenomenon to surface waves supported by the grating [38]. In 1957, Ritchie predicted both the excitation of a surface wave in metal foils in addition to bulk plasma oscillations [39]. These predictions were confirmed and such waves were termed surface plasmons. More recently plasmonics has

become a major interdisciplinary research field, which has found applications especially in the development of more efficient solar cells [40]. In this section, we present the basic theory describing propagating surface plasmons will be presented that will help to understand what is happening at the Cu/Bi_2O_3 in chapter 5.

Surface plasmons (or more precisely surface plasmon polaritons (SSP)) are known as coherent oscillations of conduction electrons on an interface between a material with negative permittivity (usually metal) and a dielectric. These oscillations will propagate along the interface between the metal and the dielectric. While the propagating plasmons have their electromagnetic field penetrating several hundreds of nanometers into the dielectric and tens of nanometers into the plasmonic metal, field of localized surface plasmons are confined to an even smaller volume (the typical penetration depth is in the order of tens of nanometers).

2.3.2 Surface plasmons on a metal-dielectric interface

A presentation of the surface plasmons at the metal-dielectric interface is shown in figure 2.6. To better understand this phenomenon, we need to start from Maxwell's equations, which can be solved for the metal and the dielectric parts.

$$\nabla \cdot \mathbf{D} = \rho \tag{2.7}$$

$$\nabla \cdot \mathbf{B} = 0 \tag{2.8}$$

$$\nabla \times \mathbf{E} = -\partial \mathbf{B}/\partial t \tag{2.9}$$

$$\nabla \times H = J + \partial \mathbf{D}/\partial t \tag{2.10}$$

which connects the macroscopic fields (dielectric displacement D, electric field E, Magnetic field H and magnetic induction B) with an external charge density ρ and current density J.

The conditions for the continuity of the normal and transversal fields at the interface can be written as (from 'Optical properties of Solids' of Fox [41])

$$D_{D,z} = D_{M,z} \qquad B_{D,z} = B_{M,z}$$

$$E_{D,x/y} = E_{M,x/y} \qquad H_{D,x/y} = H_{M,x/y}$$

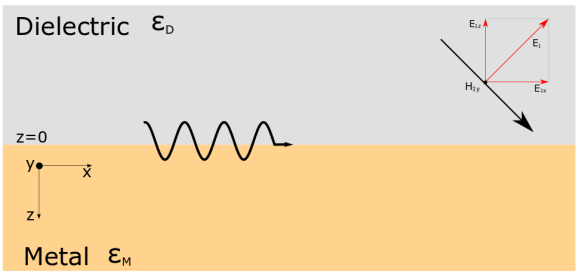

FIGURE 2.6. Interface in the x-y plane between a dielectric and a metal.

with the complex permittivity $\epsilon_M = \epsilon'_M + \epsilon''_M$ and dielectric with a permittivity ϵ_D.

When the optical constants of the materials gets the condition : $\epsilon'_M < 0$ and $\epsilon'_M < \epsilon_D$ which is for example fulfilled for copper at visible or near infrared frequencies, it is possible to find that the only guide mode supported by this structure is the transversally magnetic (TM) polarization. So it gives the following fields structures for a wave propagating in the x direction as in 2.6 :

$$\mathbf{E} = (E_x, 0, E_z) e^{i(\mathbf{k}\cdot r - i\omega t)} \tag{2.11}$$

$$\mathbf{H} = (0, H_y, 0) e^{i(\mathbf{k}\cdot r - i\omega t)} \tag{2.12}$$

$$\mathbf{D} = \epsilon_0 \epsilon_i \mathbf{E} \tag{2.13}$$

$$\mathbf{B} = \mu_0 \mathbf{H} \tag{2.14}$$

The equations above are valid for the metal and the dielectric. To have a continuity, following the Maxwell's equations :

$$\frac{k_{M,z}}{\epsilon_M} = \frac{k_{D,z}}{\epsilon_D} \tag{2.15}$$

As we describe modes that can only be at the interface. It means that the $k_{M,z}$ and $k_{D,z}$ components have to be imaginary and of opposite sign

$$k_{D,z} = +i\kappa_D \tag{2.16}$$

The fields decay exponentially into the respective half spaces : $\mathbf{E} \propto exp(\pm\kappa_D z)$. We show that in figure 2.7.
Because of the boundary conditions of equation 2.10, the surface plasmons exist only if the two dielectric constants of the materials have opposite signs. It shows that the

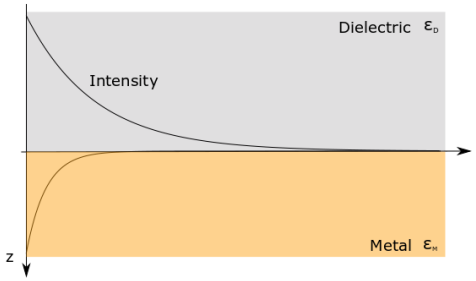

FIGURE 2.7. Evanescent field that decays exponentially into the two half spaces

surface plasmons can then only exist between the interface of metal ($\epsilon_M < 0$) and a dielectric ($\epsilon_D > 0$)

So here, an electro-magnetic wave in a dielectric medium and an oscillating electron plasma in the metal can be obtained a system. Due to this composed characteristics, surface plasmons are often referred as surface plasmon polaritons as shown in figure 2.8.

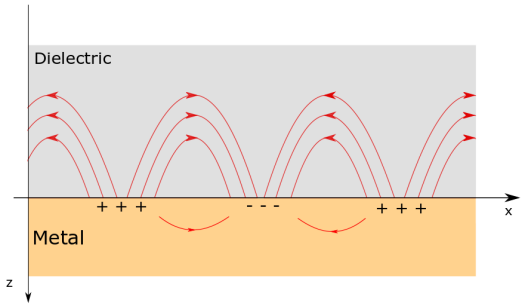

FIGURE 2.8. Surface plasmon polaritons at the interface of metal and dielectric

The plasmon propagation constant $k_x = \beta$ of this mode can be expressed as:

$$\beta = \frac{\omega}{c}\sqrt{\frac{\epsilon_M \epsilon_D}{\epsilon_M + \epsilon_D}} \tag{2.17}$$

The surface plasmon polariton dispersion curve makes the excitation of surface plasmon polariton by direct illumination of light not possible as energy and momentum conservation cannot be fulfilled at the same time. Instead, in order to excite surface plasmon polariton, a momentum transfer has to be established.

2.3.3 Excitation of surface plasmons polaritons by grating coupling

We detail here the grating coupling to excite the surface plasmon polaritons. The mismatch in wavevector between the in-plane momentum of incoming photons and k_x can be overcome by using diffraction effects such as a grating on the metal surface. As shown for example in figure 2.9, the phase matching happens when the following condition is fulfilled :

$$\beta = k \sin\theta \pm nG$$

with G = 2π/a the reciprocal vector and n an integer.

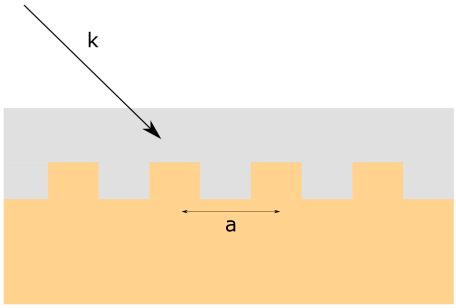

FIGURE 2.9. Grating coupling of incoming light with wave vector k on a metal grating surface of a period a

This theory will be helpful to understand the spectroscopy measurement in chapter 3.

2.4 Theory of Magnet-Optical Kerr Effects

2.4.1 Introduction

The magneto-optical Kerr effects are categorized depending on the geometry of the magnetization depending on the plane of incidence and the film plane. In the longitudinal Kerr effect, the magnetization is parallel both to the surface of the sample and the incident plane. In the polar Kerr effect, the magnetization is out of plane of the surface but in the plane of incidence. In the last case of transverse Kerr effect, the magnetization is parallel to the sample surface but perpendicular to the incident plane. These are summarized in figure 2.10.

When the magnetization vector is oriented as one of the previous cases, the incident linear polarization (green arrow in fig 2.10) is reflected by the surface and the reflected

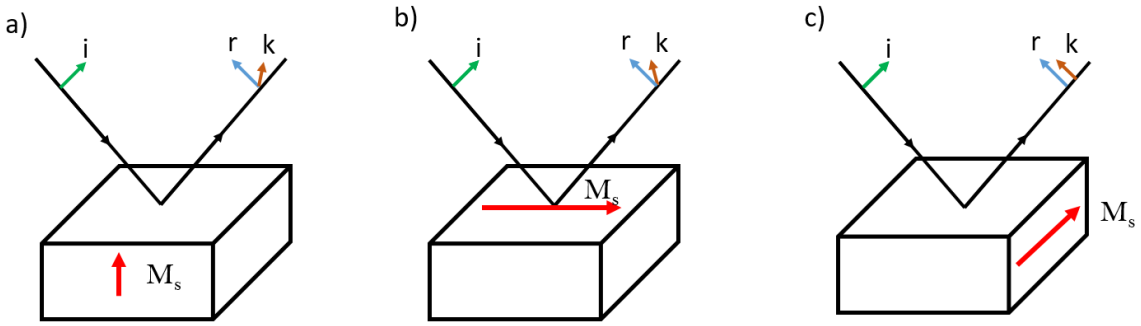

FIGURE 2.10. Different Magneto-Optical Kerr Effects (MOKE). a) Polar MOKE b) Longitudinal MOKE c) Transverse MOKE

light can be separated into two parts : The reflected linear oscillation (blue arrow in fig 2.10) but also there is an oscillation due to the Lorentz force. So, a perpendicular component known as the Kerr component represented (by the brown arrow in fig 2.10 is included in the reflected light. This means that even if depending on the polarization of the incident light, the reflected light has a different polarization or amplitude depending on the magnetization of the sample. In the following sections, we elaborate answer of the polarized light depending on the geometry of the studied system.

2.4.2 Geometries of Kerr effect

As mentioned previously, there are three different geometries of MOKE where their differences are relative to the plane of light incidence. These three different geometries of MOKE are shown in figure 2.10 consist in the polar MOKE, longitudinal MOKE and transverse MOKE. The change of polarization and amplitude are described by the follozing figure 2.11

In the figure 2.11, the major axis of the ellipse is slightly rotated with respect to the principal plane and is referred as the Kerr rotation. All in all, The Kerr rotation θ_k and ellipticity ϵ_k can be expressed as

$$\theta_k + i\epsilon_k = R_k/R_n \tag{2.18}$$

Understanding this equation, we detail R_k and R_n depending on the geometry.

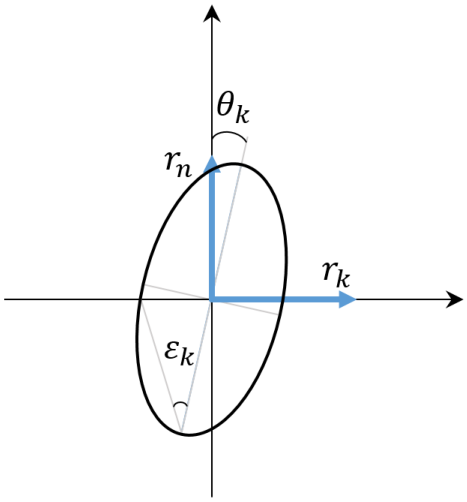

FIGURE 2.11. Geometry of the Kerr rotation θ_k and ellipticity ϵ_k

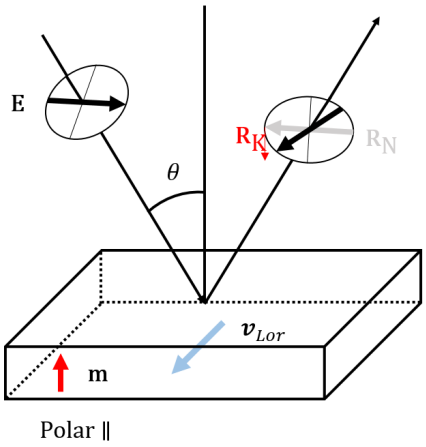

FIGURE 2.12. Schematic of the polar MOKE. The magnetization **m** is perpendicular to the surface of the studied sample, the incident light is linearly polarized and oscillating in parallel to the plane of polarization

2.4.2.1 Polar MOKE

In the polar MOKE configuration, the magnetization **m** is perpendicular to the surface of the studied sample, the incident light is linearly polarized and oscillating in parallel to the plane of polarization. Figure 2.12 shows $\mathbf{R}_N$, the regularly reflected light where the polarization is also in the incident plane. As said in previously, a small vibration

is induced by the Lorentz force v_{Lor} perpendicularly to the electric field and the magnetization direction. This secondary motion is proportional to the Lorentz movement (-$\mathbf{m} \times \mathbf{E}$) and generates the Kerr amplitude $\mathbf{R}_K$ for reflected light. The difference in angle between $\mathbf{R}_N$ and $\mathbf{R}_K$ results in the magnetization dependent polarization rotation. From this simple observation, we can understand that the Kerr effect in a polar system is the strongest at normal incidence ($\theta = 0°$).

2.4.2.2 Longitudinal MOKE

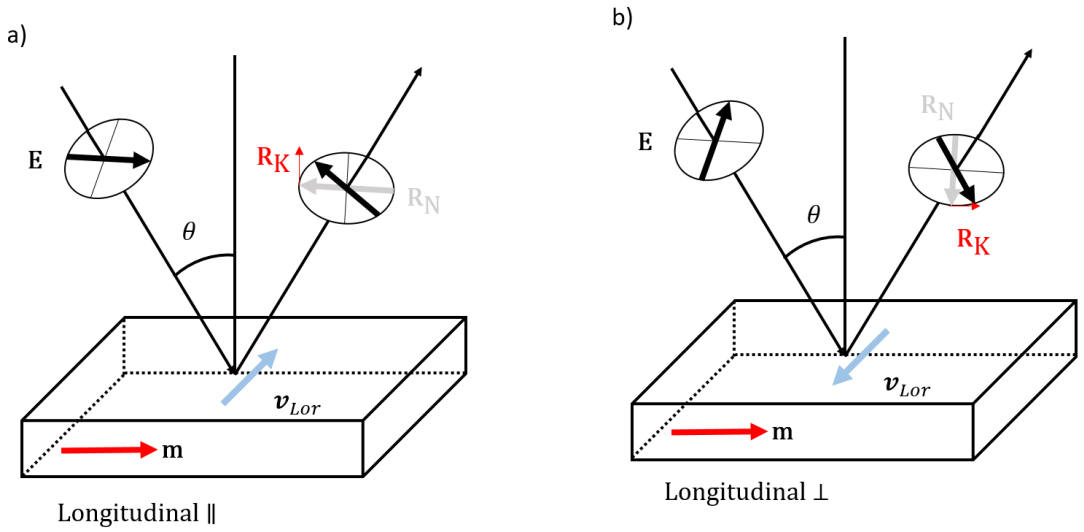

FIGURE 2.13. Schematic of a) parallel and b) perpendicular plane of the longitudinal geometry relative to the plane polarization of the light.

For the longitudinal geometry, the magnetization direction of the sample is parallel to the plane of light incidence. The longitudinal effect induces rotational change to the plane of polarization for both parallel polarization and the perpendicular polarization plane of incident light. As it can be seen in figure 2.13, the Lorentz motions (v_{Lor}) in the two different polarizations of the plane of incidence are opposite to each other depending on the polarization. It gives an opposite rotational direction of the resulting Kerr amplitude. Also as opposed to the polar configuration, the longitudinal effect disappears for normal light incidence ($\theta = 0°$) as the Lorentz force vanishes.

2.4.2.3 Transversal MOKE

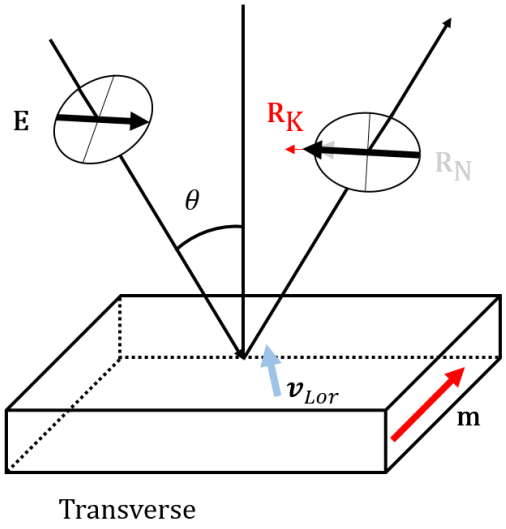

FIGURE 2.14. Schematic of the transverse MOKE. The magnetization direction is perpendicular to the plane of light incidence.

In the transverse MOKE geometry, the magnetization direction is perpendicular to the plane of light incidence. As shown in the Figure 2.14, v_{Lor} is now out of plane, so the transverse effect causes amplitude change to the reflected light but the polarization direction of the Kerr amplitude is the same as that of the regularly reflected light. So, as opposed to the polar and longitudinal MOKE, transverse MOKE measures the intensity and not the polarization. However, similar to the longitudinal MOKE, the transverse effect is eliminated in normal incidence to the sample surface.

2.4.3 Phenomenological Model of Kerr Effect

The model of the Kerr effect is described phenomenologically by the off-diagonal permittivity tensor with off-diagonal elements. These elements depend on the Voigt magneto-optical parameter Q that describes the interaction of the electromagnetic field with the electrons of studied material .
The permittivity tensor can be written from:

$$\epsilon' = \begin{pmatrix} \epsilon'_{xx} & \epsilon'_{xy} & \epsilon'_{xz} \\ \epsilon'_{xy} & \epsilon'_{yy} & \epsilon'_{yz} \\ \epsilon'_{xz} & \epsilon'_{xz} & \epsilon'_{zz} \end{pmatrix} + i \begin{pmatrix} 0 & -\epsilon''_{xy} & \epsilon''_{xz} \\ \epsilon''_{xy} & 0 & -\epsilon''_{yz} \\ -\epsilon''_{xz} & \epsilon''_{xz} & 0 \end{pmatrix} \tag{2.19}$$

even in **m** odd in **m**

If we assume a magnetization vector **m** in the z-direction, we can simplify the tensor :

$$\epsilon'_{xz} = \epsilon'_{yz} = \epsilon''_{xz} = \epsilon''_{yz} = 0$$
$$\epsilon'_{xx} = \epsilon'_{yy} = \epsilon'$$
$$\epsilon'_{zz} = \epsilon'_0 = (n - i\mathrm{k})^2 = \mathrm{n}^2$$

where n is the refractive index and k is the principal absorption coefficient. It is then possible to rewrite the tensor depending on Q :

$$\epsilon' = \begin{pmatrix} \epsilon' & -i\epsilon' Q & 0 \\ i\epsilon' Q & \epsilon' & 0 \\ 0 & 0 & \epsilon'_0 \end{pmatrix} \tag{2.20}$$

Definition of ϵ'

The diagonal components of the permittivity tensor ϵ'_{xx} and ϵ'_{yy} are rewritten here ϵ' because of the symmetry consideration are also function of the magneto-optical parameter Q. Experiments [42] show that Q is very small ($Q \ll 1$) so it is possible to expand the tensor ϵ' in the power of Q

$$\epsilon'(Q) = \epsilon'_0 + \left(\frac{\partial \epsilon'}{\partial Q}\right)_{Q=0} Q + \frac{1}{2}\left(\frac{\partial^2 \epsilon'}{\partial Q^2}\right)_{Q=0} Q^2 \tag{2.21}$$

When the direction of the magnetization vector is reverse, the equation above becomes

$$\epsilon^{'}(-Q) = \epsilon^{'}_0 - \left(\frac{\partial \epsilon^{'}}{\partial Q}\right)_{Q=0} Q + \frac{1}{2}\left(\frac{\partial^2 \epsilon^{'}}{\partial Q^2}\right)_{Q=0} Q^2 \tag{2.22}$$

We know that with $\epsilon^{'}(Q) = \epsilon^{'}(-Q)$ because the electric displacement field $\mathbf{D} = \epsilon^{'}\mathbf{E}$ must be invariant under magnetization reversal.

So $\epsilon^{'}(Q)$ becomes

$$\epsilon^{'}(Q) = \epsilon^{'}_0 + \frac{1}{2}\left(\frac{\partial^2 \epsilon^{'}}{\partial Q^2}\right)_{Q=0} Q^2 = \epsilon^{'}_0 + \epsilon^{'}_0 f Q^2 \text{ with } f = \frac{1}{2\epsilon^{'}_0}$$

so we understand that $\epsilon^{'}$ is even in Q, and has no contribution to the Kerr effect. By ignoring the Q^2, we have $\epsilon^{'} = \epsilon^{'}_0$

So the permittivity tensor now becomes for **M** parallel to the z-axis :

$$\epsilon^{'} = \begin{pmatrix} \epsilon^{'}_0 & -i\epsilon^{'}_0 Q & 0 \\ i\epsilon^{'}_0 Q & \epsilon^{'}_0 & 0 \\ 0 & 0 & \epsilon^{'}_0 \end{pmatrix} \tag{2.23}$$

The off-diagonal components of the permittivity tensor are proportional to the resultant magnetization. Then, Q gives all the magneto-optical Kerr effects.

2.4.4 Kerr Fresnel reflection coefficients

The explanation for longitudinal and transverse Kerr effect above can be simplified by using the Kerr Fresnel reflection coefficient that has been obtained by applying Maxwell boundary conditions at surface films [43]. Referring to Figure 2.16 which shows p-polarized light that is incident to the surface and then gets reflected, the coefficients for longitudinal Kerr effect can be written such as [43] :

$$r^l_{pp} = \frac{n\cos\theta - \left(1 - \frac{\sin^2\theta}{n^2}\right)^{\frac{1}{2}}}{n\cos\theta + \left(1 - \frac{\sin^2\theta}{n^2}\right)^{\frac{1}{2}}} \tag{2.24}$$

$$r^l_{pp} = \frac{\cos\theta - n\left(1 - \frac{\sin^2\theta}{n^2}\right)^{\frac{1}{2}}}{\cos\theta + n\left(1 - \frac{\sin^2\theta}{n^2}\right)^{\frac{1}{2}}} \tag{2.25}$$

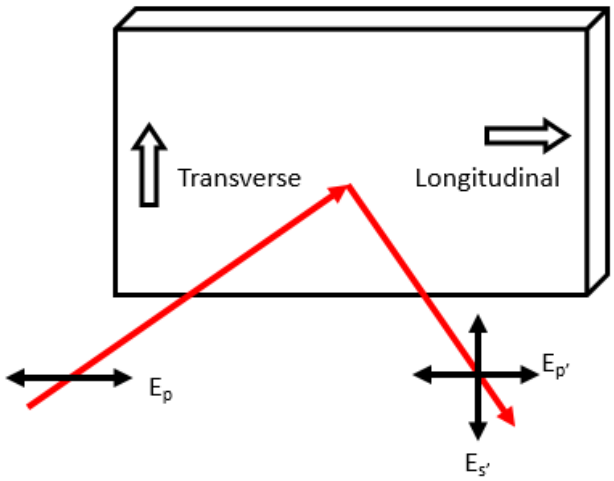

FIGURE 2.15. Kerr Fresnel reflection coefficients with p-polarized incident light that is incident to the surface and then gets reflected

$$r_{ps}^{l} = r_{sp}^{l} = \frac{\sin\theta\cos\theta k}{\left(n\cos\theta + \left(1 - \frac{\sin^2\theta}{n^2}\right)^{\frac{1}{2}}\right)\left(\cos\theta + n\left(1 - \frac{\sin^2\theta}{n^2}\right)^{\frac{1}{2}}\right.} \tag{2.26}$$

And the Fresnel reflection coefficient for the transverse Kerr effect is :

$$r_{pp}^{t} = \left(\frac{n\cos\theta - \left(1 - \frac{\sin^2\theta}{n^2}\right)^{\frac{1}{2}}}{n\cos\theta + \left(1 - \frac{\sin^2\theta}{n^2}\right)^{\frac{1}{2}}}\right)\left(1 + \frac{ksin(2\theta)}{n^2(n^2cos^2\theta - 1) + sin^2\theta}\right) \tag{2.27}$$

$$r_{ss}^{t} = \frac{\cos\theta - n\left(1 - \frac{\sin^2\theta}{n^2}\right)^{\frac{1}{2}}}{n\cos\theta + \left(1 - \frac{\sin^2\theta}{n^2}\right)^{\frac{1}{2}}} \tag{2.28}$$

$$r_{ps}^{t} = r_{sp}^{t} = 0 \tag{2.29}$$

With θ the angle of incidence at the normal of the sample, $k = i\epsilon^{'}Q$ the off-diagonal element of the permittivity tensor shown 2.23. Looking at the longitudinal Kerr effect, the coefficients confirm that there is a magnetic-dependent rotational change to the plane polarization of the incident light by the derived off-diagonal terms in Equation 2.26. However, for the transverse coefficients above, the transverse Kerr effect does not cause a rotational change to the plane of polarization of the incident light given that the off-diagonal terms which cause the rotational are equal to zero as shown in Equation 2.29. The only parameter that is magnetization-dependent is the reflection coefficient related to the incident and reflected p-polarised light given in Equation 2.27. Therefore there will only be light intensity and phase change (which is the ellipticity) due to for transverse effect as shown previously.

We treated here the common case of polarization in plane for the transverse geometry, but an experimental report [44] demonstrated that by using a mixed state of s- and p- polarization enhances the Kerr effect signal in transverse MOKE configuration. We will expand our discussion about this report in Chapter 4.

2.5 Light polarization state

Lasers are usually producing linearly polarized light. However it is also practicable to create circularly and elliptically polarized radiation. However, the degree and the character of the polarization is a major parameter for the investigation of the photocurrents and the effects of the samples and interfaces we are going to study. The polarization can be manipulated by reflection, with dichroic and birefringent crystals. In this work birefringent crystals were implemented to change the state of polarization by $\lambda/4$ and $\lambda/2$ plates.
To describe an exact state of polarization, the Stokes parameters S_0, S_1, S_2 and S_3 are defined. S_0 represents the total light intensity. By assuming the light propagating in the z-direction, the parameter S_1 is defined as the light intensity of the linear polarized radiation in x-direction subtracted by the one in the y-direction. S_2 equals the light intensity of linear polarization at +45° subtracted by the one at -45° and S_3 represents the light intensity of left-circular polarization subtracted by the intensity of the right-circular polarization. So, the Stokes parameters describe every state of polarization by the relative difference of the intensity components. An alternative approach to describe the Stokes parameters can be via the component of the electric field in x- and y- directions.

Therefore, the Stokes parameters can be summarized :

$$
\begin{aligned}
S_0 &= I_x + I_y = |E_x|^2 + \left|E_y\right|^2 = |E|^2 \\
S_1 &= I_x - I_y = |E_x|^2 - \left|E_y\right|^2 \\
S_2 &= I_{+45^\circ} - I_{-45^\circ} = E_x E_y^* + E_x^* E_y \\
S_3 &= I_R - I_L = i(E_x E_y^* - E_x^* E_y)
\end{aligned}
$$

Furthermore, the Stokes parameters can be exactly identified by a series of polarization filters taking the different linearly and circularly polarization states into account. To tune the light polarization state birefringent crystals are used in the experiment to switch from one state to another. In general, the direction of propagation of an electromagnetic wave is different for unequal directions in an anisotropy crystal depending on the crystal axis. If a parallel unpolarized light beam hits a crystal, the part polarized perpendicular to the optical axis of the crystal $E_\perp$ follows the Snell's law and is called ordinary axis. The orthogonally polarized part $E_\parallel$, does not and therefore is called the extraordinary axis. Due to different dielectric constants, two different propagation velocities and refractive indexes during the transit process. This allows to influence the light polarization state by specific retardation and allow to obtain either linear, circular or elliptical polarized light.
One applied polarizer is a $\lambda/4$. $\lambda/4$ offers the possibility to get elliptical and even circular polarized light out from the linear polarized light. This is done by a birefringent coplanar crystal plate with the optical axis is placed orthogonal to the incoming beam. The wave experiences different refractive indexes n in the two dimensions of the plate and it leads to a different optical path Δl and a phase shift $\Delta\varphi$ which both are dependent on the wavelength and the thickness of the plate which can be expressed as

$$
\begin{aligned}
\Delta l &= d\Delta n \\
\Delta\varphi &= \frac{2\pi}{\lambda_0} d\Delta n
\end{aligned}
$$

If the thickness d is correctly chosen in a way that $d\Delta n = m\lambda_0 + \frac{\lambda_0}{4}$ (m is an arbitrary integer), a phase shift $\Delta\varphi = \frac{\pi}{2}$ occurs. Then, the $\lambda/4$-plate transforms the light radiation, which is linearly polarized into an exact circularly polarized light at an angle of 45° degree to the optical axis. In the cases that the angle between the optical axis and th polarization direction are not a multiple of 45°, the light is elliptically polarized. A schematic of the polarization states depending on the different angles between the incoming beam and the optical axis of the crystal is shown in figure 2.16.

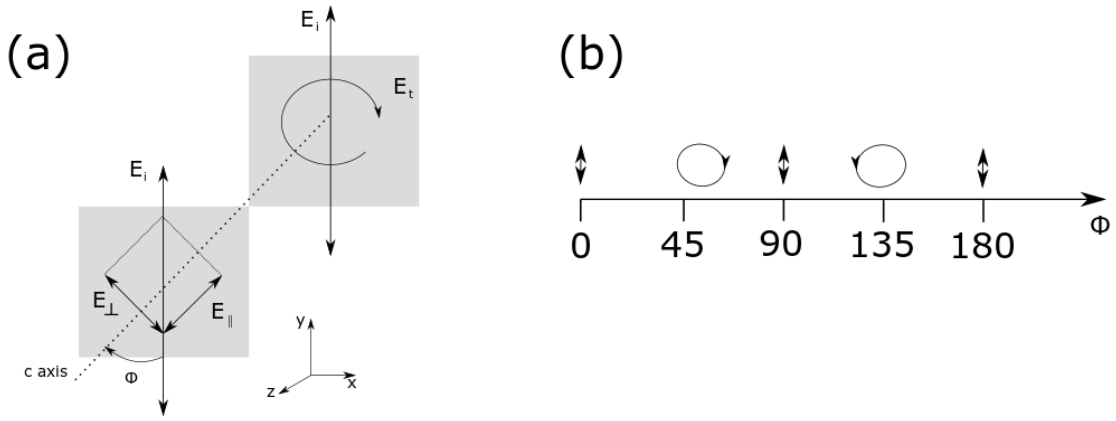

FIGURE 2.16. (a) Sketch of a λ/4-plate with initial and final polarizations (b) degree of polarization depending on ϕ

By assuming a polarized wave propagating along the negative z-direction and normalizing the Stokes parameters S_0, S_1,S_2 and S_3 to the total intensity S_0 the Stokes parameters finally becomes :

(2.30) $$S_0 = I_{total}$$

(2.31) $$S_1 = -\cos^2 2\varphi$$

(2.32) $$S_2 = \frac{\sin 4\varphi}{2}$$

(2.33) $$S_3 = P_{circ} = -\sin 2\varphi$$

For the right-handed circular polarization (σ_+) $P_{circ} = -\sin 2\varphi$ equals +1. For the left-handed circular polarization (σ_-) P_{circ} is equals to -1.

CHAPTER 3

SAMPLE PREPARATION AND CHARACTERIZATION

In this section, we summarize the fabrication processes of our samples. Then, we introduce the used characterization methods such as atomic force microscope (AFM), Energy dispersive X-ray spectroscopy (EDX), X-ray diffraction (XRD) and optical spectroscopy.

3.1 Sample fabrication

3.1.1 Steps of fabrication

Samples were fabricated following the steps which are sketched in figure 3.1. At first, Si/SiO_2 wafers were cut into 10 to 20 mm square pieces (figure 3.1(a)). Then, the photosensitive resist was spin coated to make patterns using maskless photolithography (figure 3.1 (b) and (c)). Either non-magnetic metal/oxide or titanium/gold were deposited using e-beam evaporation (figure 3.1 (d)). After this step, lift-off and cleaning were done (figure 3.1 (d)). Detailed steps are described in the following sections.

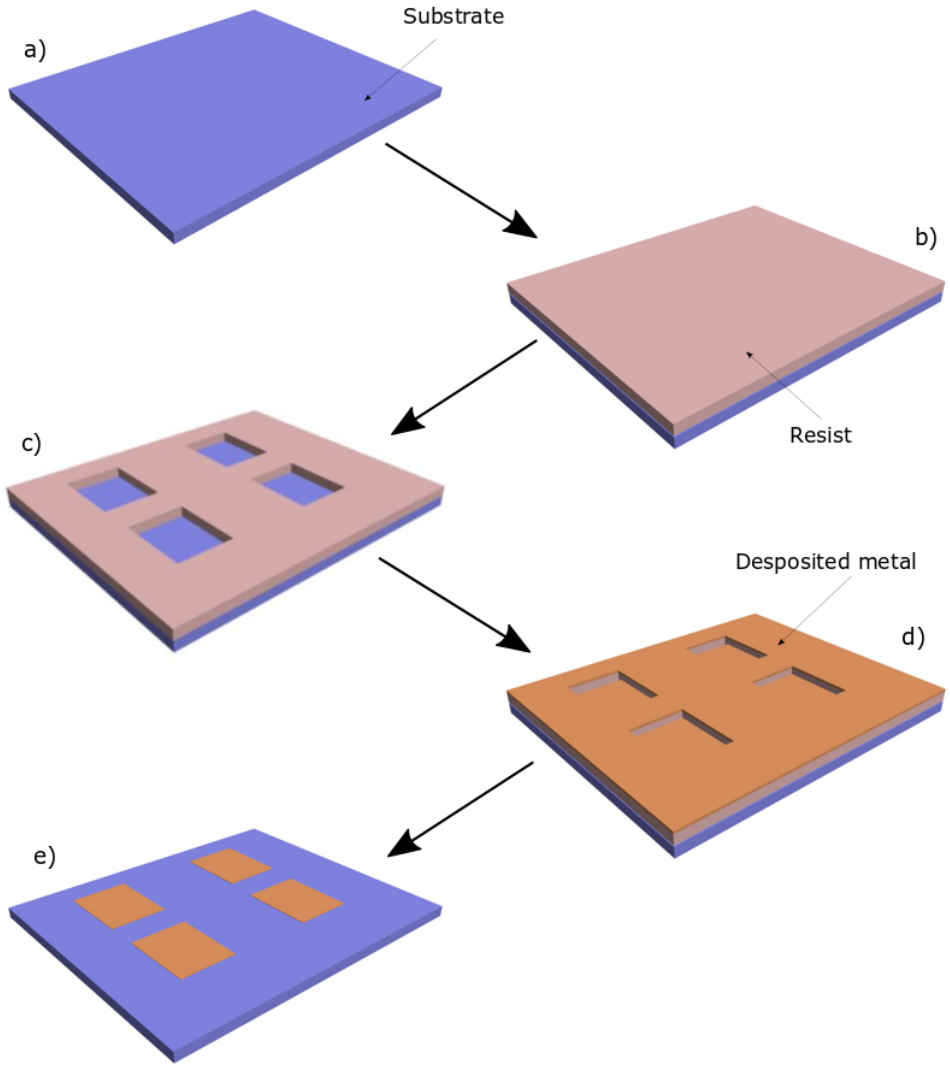

FIGURE 3.1. Schematic illustration of lithography and lift-off process of positive resist

3.1.2 Maskless photo-lithography

Maskless photo-lithography is a powerful fabrication technique for experimentalists. It enables patterning at micrometer scale. In this study, we used a maskless UV photo-lithography D-Light-DL100RS system in which the position of the laser is controlled by mirrors. Patterning process is described as follow :

1. Si substrate with 300 nm SiO_2 layer on top is cut in pieces using a scriber with a dimension of either 10 or 20 mm.

2. Cleaning of the substrate: the substrate is plunged into acetone and put in an ultrasonic bath for 15 min then dried with an airgun. Then, the substrate is cleaned briefly in IPA (isopropyl alcohol) and dry again with an airgun. Then, a last cleaning using ultraviolet is done for 5 min to remove all the organic on the surface. In the end, the sample, is checked by an optical microscope to verify its cleanliness.

3. (1,1,1,3,3,3,-Hexamethyldisilazane, $C_6H_{10}NSi_2$, HDMS) typically used to make the resist stick to sample more easily, is spin-coated at 500 rpm for 5 seconds then 5000 rpm for 40 seconds.

4. The sample is baked in an oven at 80°C for 5 minutes.

5. The sample is cooled down at room temperature for 2 min then AZ1500 resist is spin-coated at 500rpm for 5 seconds then 5000 rpm for 40 seconds.

6. The sample is baked in an oven at 80°C for 10 minutes.

7. The sample is exposed using photolithography at 95 mJ/mm^2.

8. Patterns are developed for 45 seconds and rinsed in flowing water for 1 minute.

9. The sample pattern is checked by an optical microscope.

3.1.3 Deposition

We used an electron beam system to evaporate our material. Table 3.1 shows the different pressures and deposition rates of each materials we deposited during this thesis.

Material	Pressure (Pa)	Rate (Å/s)
Cu	$6.3\ 10^{-6}$	1.0
Ag	$7.2\ 10^{-6}$	1.0
Bi_2O_3	$1.6\ 10^{-5}$	0.2
Ti/Au	$1.0\ 10^{-4}$	2.5
SiO_2	$6.3\ 10^{-6}$	0.2
Al_2O_3	$2.2\ 10^{-6}$	0.2

TABLE 3.1. Material deposition pressures and rates

3.1.4 Lift-off

After the deposition, resist is removed by soaking the sample in acetone using ultrasonic until the all the resist is removed which usually takes one to two minutes. a

3.2 Sample Characterization

3.2.1 Atomic Force Microscopy

3.2.1.1 General principle

The Atomic Force Microscope (AFM) is a scanning probe microscope that can achieve a topographical image of the sample surface based on the interactions between a tip and a sample surface. AFM was invented by Gerd Binning et al. in 1986 [45] based on Scanning Tunneling Microscope technique (STM). While STM can only measure conductive samples, AFM technique can measure any type of sample

A typical AFM consists of a cantilever with a small tip at the end, a diode laser, a 4-quadrant photodiode and a piezoelectric scanner, as shown in figure 3.2. Analysis of the inflection of the cantilever through the surface with the laser probe and the photodetector allows detecting the exact record of the tip motion. Measurement of interactions forces between the tip and the sample surface gives the possibility to probe surface characteristics with accurate resolution in a range of 100 μm to 200 nm.

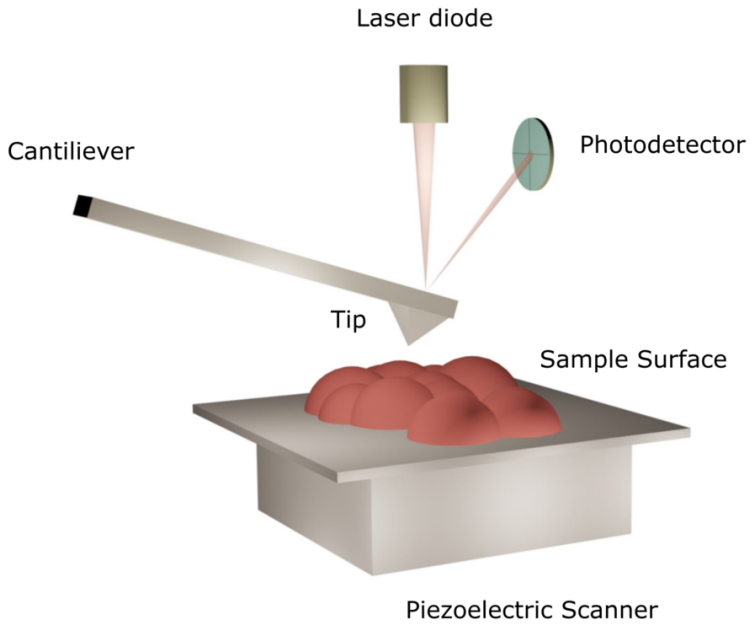

FIGURE 3.2. Schematic of atomic force microscopy measurement. Analysis of the inflection of the cantilever through the surface with the laser probe and the photodetector allows detecting the exact record of the tip motion.

3.2.1.2 Measurement of samples using AFM

We measure the roughness of our sample using an AFM for Cu(10 nm), Cu(20 nm) and Cu(30 nm)/Bi_2O_3 (20nm) surfaces. The goal of this study is to check the interface roughness as it is an essential parameter to understand the conversion at the Rashba interface. Typical results of AFM measurements are shown in figure 3.3 and the average roughnesses of our multiple measurements is presented table 3.2.

Surface	Roughness Average (nm)	Root mean square (nm)
Cu(10 nm)	1.0	1.2
Cu(20 nm)	0.7	0.9
Cu(30 nm)/Bi_2O_3(20 nm)	1.4	1.9

TABLE 3.2. Roughness average and root mean square of the scanned surface

We used the lowest possible resolution of 200 × 200 nm. Figure 3.3 (b) and 3.3 (e) show respectively the AFM image of Cu with a thickness of 20 nm and 10 nm. In order to avoid as much as possible the oxidation of copper, the samples were measured approximately

during 10 min to 20 min after deposition, which gives an unavoidable oxide layer of 0.7 nm[46] in our current setup system. On average, the Cu(10 nm) sample is rougher by 30% when compared to Cu(20 nm) and root-mean-square is on average 25% higher on Cu(10 nm) compared to Cu(20 nm). Also, some 'islands' can be seen at the surface of both Cu at 10 nm and 20 nm in figure 3.3 (b,e), indicating the possibility of light excited plasmon states. Z.Yang et al.[47] results show that the surface plasmon resonance in gold is sensitive to the root-mean-square roughness, and it gradually decreases by reducing the surface root-mean-square roughness. These AFM results will be essential to understand our experiments explained in chapter 5. As a reference, we also measured the AFM of Cu(30 nm)/Bi_2O_3(20 nm), shown figure in 3.3 (g) that show increasing of the surface roughness and RMS compared to Cu(20 nm). A possible explanation of this increasing of roughness in Cu/Bi_2O_3 compared to Cu is that the oxide deposition process leads to a high surface density of crystallization centers, with different growth directions and rates. These results in nanocrystallites of different dimensions and geometrical shapes. The existence of the nanocrystallites for Bi_2O_3 has been experimentally proved previously by Leontie et al. [26].

3.2.2 Energy-dispersive X-ray spectroscopy

3.2.2.1 General principle

Energy-dispersive X-ray spectroscopy (EDX) is also a common analytical technique used for chemical characterization of a sample. It uses an X-ray excitation source and a sample. The main characteristic of this measure is that each atom has a unique atomic structure, so it gives a unique set of peaks on its electromagnetic spectrum. In order to stimulate the emission of a sample, a beam of charged electrons at high-energy is focused on the sample studied. At rest, the electrons of the samples are at ground state bounded to the nucleus. The incident beam will excite the electron of an inner shell and eject them. Then, electrons with higher energy state will replace them and emit radiation that will be detected. A schematic summarizing the effect is shown figure 3.4.

3.2.2.2 Measurement

We used a Rigaku EDXL300 and did measurements on Cu/Bi_2O_3 and Ag/Bi_2O_3 using four different excitation sources (RX9, Cu, Mo, Al) as each target can detect a certain range of energies. The properties of these targets are summarized in table 3.3.

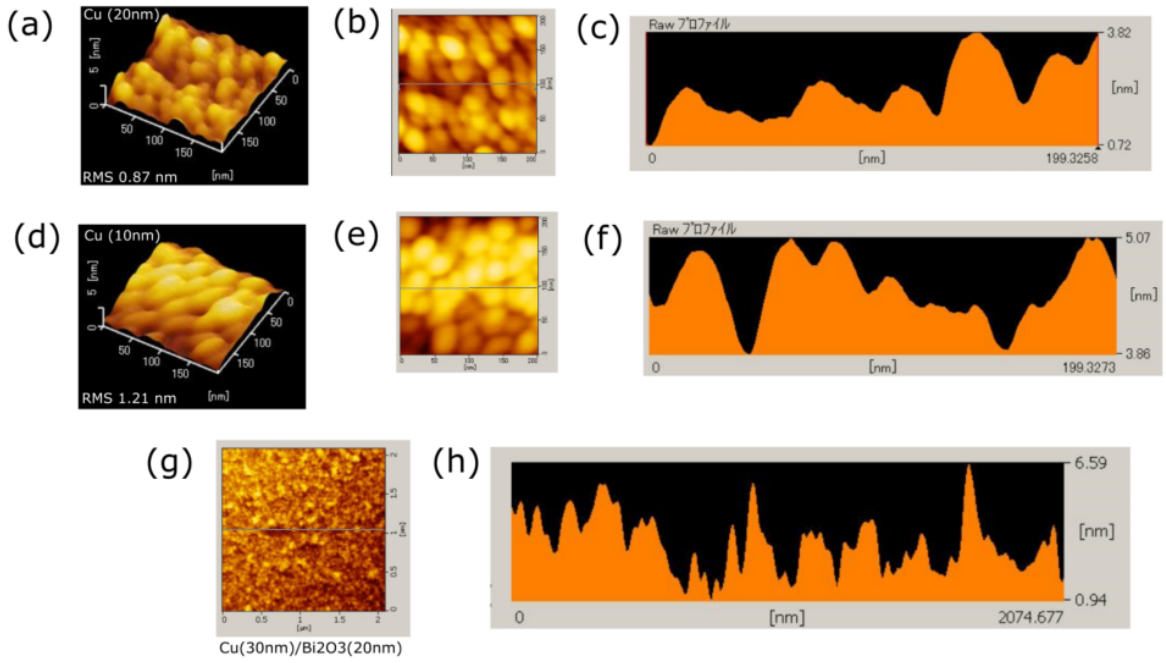

FIGURE 3.3. Atomic force microscopy of (a-c) Cu(20 nm) (d-f) Cu(10 nm) and (g-h) Cu(20 nm)/Bi_2O_3(20 nm). (a,d) 3D representation of the surface roughness of Cu(20 nm) and Cu(10 nm). (b,e) AFM image of 200x200 nm of Cu(20 nm) and Cu(10 nm). (c,f) Line cut of the AFM image. (g) AFM image of 2x2 μm of Cu(30 nm)/Bi_2O_3(20 nm). (f) Line cut of the AFM image.

From the table 3.3, we can understand that all the materials we want to detect can be detected with an energy range of 2 to 10 keV. Figure 3.5 (a) shows the result for Cu/Bi_2O_3 and Figure 3.5 (b) shows the result for Ag/Bi_2O_3 within this range. Peaks were identified using the EDXL300 included software. Bi-M_α transition lies around 2.3 keV, Ag-L_α lies around 3.0 keV and Cu-K_α lies around 8.0 keV.

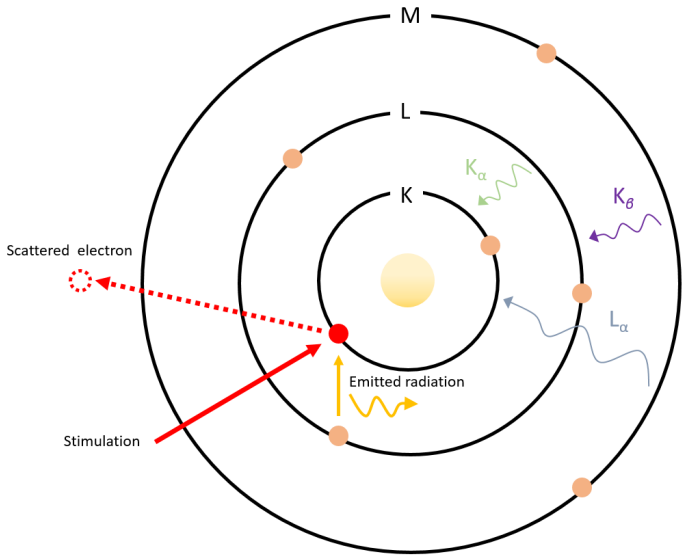

FIGURE 3.4. Principle of EDX. High-energy beam stimulation ejects an electron from the inner shell of the atom structure. An outer electron fills the hole created and emit a specific radiation.

Target	RX9	Cu	Mo	Al
Excited X-ray	Pd-L	Cu-K	Mo-K	Polarized white Xray
Range of measured elements	$_{11}$Na ~$_{17}$Cl (K-Line) $_{30}$Zn ~$_{42}$Mo (L-Line) $_{78}$Pt ~$_{83}$Bi (M-Line)	$_{19}$K ~$_{24}$Cr (K-Line) $_{47}$Ag ~$_{65}$Dy (L-Line)	$_{25}$Mn ~$_{39}$Y (K-Line) $_{60}$Nd ~$_{92}$U (L-Line)	$_{40}$Zr ~$_{60}$Nd (K-Line)
Range of Energy	1~4KeV	2~8KeV	4~15KeV	15~40KeV

TABLE 3.3. Properties of EDX Rigaku EDXL300 : Target, excited X-ray, range of measurable elements, range of energies

3.2.3 X-ray diffraction

3.2.3.1 Principle

X-ray diffraction is a non-destructive technique useful to determine the structural properties of a crystal. It relies on the Bragg condition that maximizes the density of a

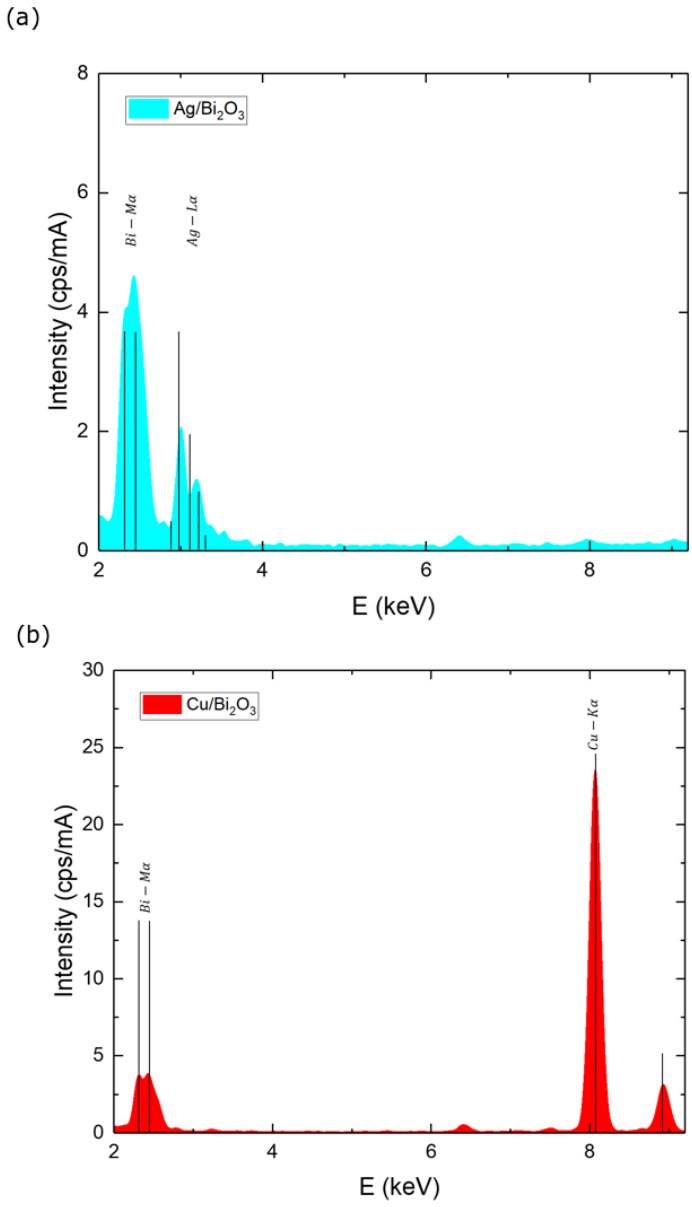

FIGURE 3.5. EDX of (a) Ag/Bi_2O_3 and (b) Cu/Bi_2O_3 in an energy range between 2keV and 9.5keV

diffraction beam at a particular angle

$$n\lambda = 2d\sin\theta \tag{3.1}$$

where n represents the order of diffraction, λ the X-ray wavelength, d the interplanar spacing and θ the angle of incidence of the X-rays. The diffraction of plane wave of

successive planes of a crystal structure is shown figure 3.6.

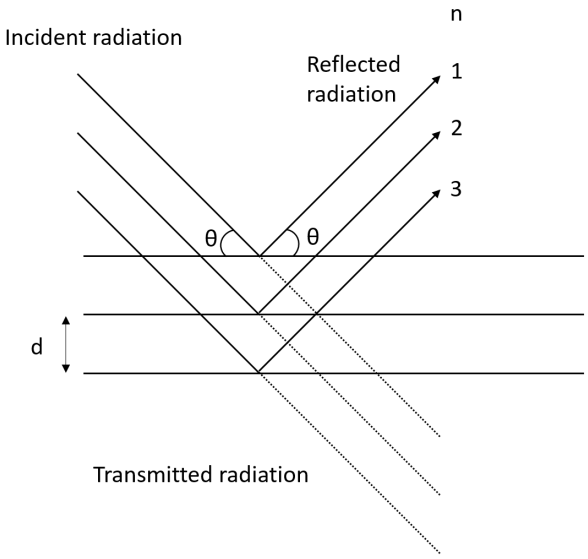

FIGURE 3.6. Bragg diffraction of X-rays by planes in a crystal at an angle θ and the planes are separated by a distance d

3.2.3.2 Measurement

In order to confirm the crystalline information at Cu/Bi_2O_3 and Ag/Bi_2O_3 interfaces, X-ray diffraction were done using a Rigaku SmartLab using Cu-K_α wavelength using grazing incidence technique. Grazing incidence technique sets the X-ray source at a fixed angle ω (angle between the incident beam and the sample surface) and the detector at an angle 2θ between the incident beam and diffracted beam. Divergence, anti-scatter and receiving slits are there to enhance the signal detected on a wider surface as shown in figure 3.7 (a). In figure 3.7 (b), if ω_1 and ω_2 are well selected, it is possible to probe the interface as the volume studied can be modified using grazing incidence technique. In figure 3.8 a) and 3.8 (b), we show respectively a XRD measurement of samples of Cu/Bi_2O_3 and Ag/Bi_2O_3 at ω_1=0.3° and ω_2=0.4°. At ω=0.3° (black lines in figure 3.8 (a) and (b)), only a peak at 28° is displayed. It represents α-Bi_2O_3. However, as the peak is relatively broad, we can conclude that α-Bi_2O_3 is mostly amorphous. At ω=0.4° (red lines in figure 3.8 (a) and (b)), the α-Bi_2O_3 peak is still there but new peaks appear. For figure 3.8 (a), two sharps peaks at 43.6° and 51.2° are shown. They can be identified as Cu(111) and Cu(100). Its sharpness compared to the peak of α-Bi_2O_3 shows that a preferal orientation in (111) direction. Similarly, 3.8 (b) shows also two peaks at 38.3°

and 44.7° representing respectively Ag(111) and Ag(100). These results show that the preferential orientation for the interface is (111), which is similar to the orientation in previous reports of Rashba interfaces of Ag (111)/Bi [23].

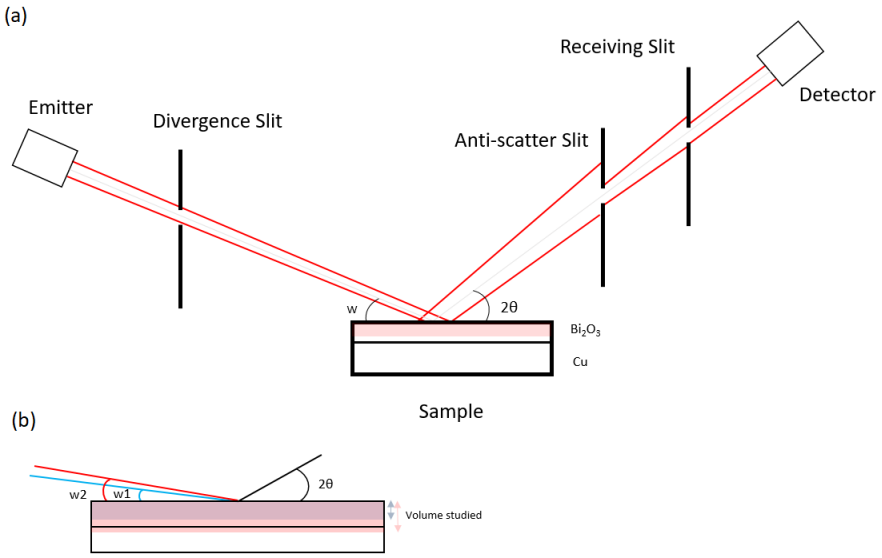

FIGURE 3.7. XRD spectroscopy at grazing incidence configuration. a) The X-ray source is at an angle ω (angle between the incident beam and the sample surface), and the detector at an angle 2θ between the incident beam and diffracted beam. b) Schematic of the difference between two grazing angles ω_1 and ω_2, showing the possibility to probe the interface.

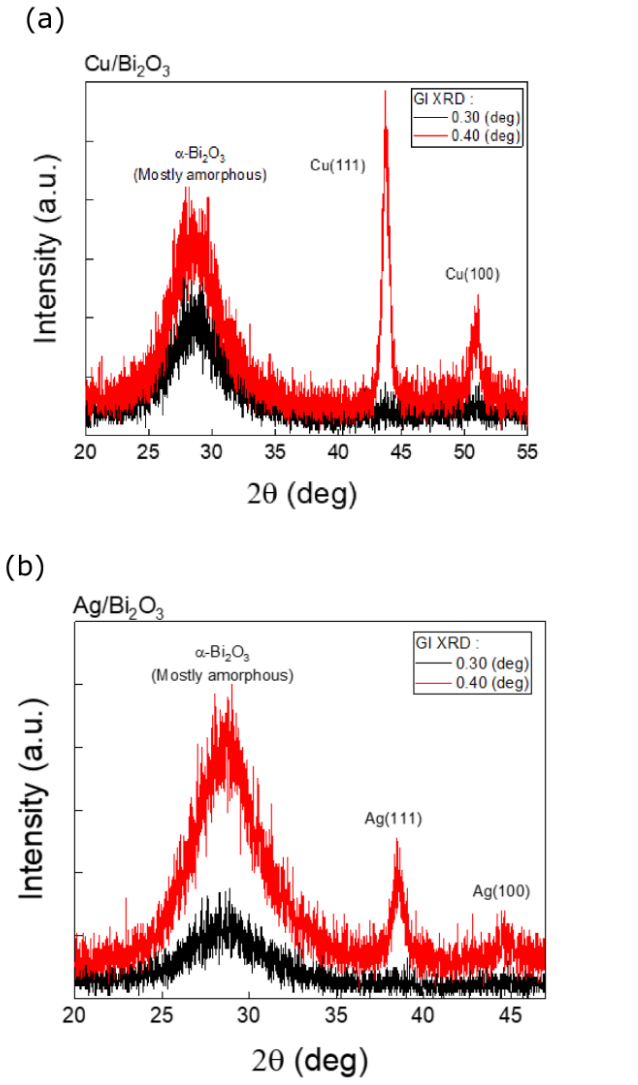

FIGURE 3.8. XRD spectroscopy characterization of a) Cu/Bi_2O_3 at 0.3° (black line) and 0.4° (red line). b) Ag/Bi_2O_3 at 0.3° (black line) and 0.4° (red line).

3.2.4 Optical spectroscopy of Cu/Bi_2O_3

We measured the optical properties of Cu/Bi_2O_3 and Cu/SiO_2 grown on Sapphire (0001) substrate using a UV-VIS-NIR spectrophotometer with integrating sphere technique. It allows measuring either the diffuse transmittance or reflectance in the range from 0.8 eV to 6.2 eV (200 nm to 1500 nm).

3.2.4.1 Optical spectroscopy of Cu and Bi_2O_3 grown separately on Sapphire(0001)

We first measured diffuse transmittance and reflectance of reference samples of a thin film of 30nm of Cu and 20nm of Bi_2O_3. Figure 3.9 (a) shows the reflectivity and transmittance of Cu 30nm. As we can see from this result, the reflectivity of copper drops quickly around 2eV. This is consistent with the data shown in Fox book [41]. Indeed, copper has an electronic configuration of [Ar]$3d^{10}4s^1$. Outer 4s bands can be approximated to free electron states with a dispersion of $E = \hbar^2k^2/2m_0$, and it can be seen as a broad band covering a large range of energies. The 3d bands are the more tightly bounded and are relatively dispersionless, thus occupying a small range of energies. Based on the Drude model the plasma frequency of copper is 10.8 eV (115 nm), copper should be totally reflective below this energy. An explanation of this drop of reflectivity can be explained by the inset of figure 3.9 (a). The eleven valence electrons fill the 3d band and half of the 4s bands of copper. So as shown in the inset, the Fermi level is located at half of the 4s band. As so, it proves that interband transitions between the filled 3d band to the unoccupied 4s band above the Fermi level is possible above a certain energy threshold. Moreover, from calculations of the exact band structure of Cu [41], this optical transition lies around 2eV, which is the reason for the sharp decreasing of reflectivity. Figure 3.9 (b) shows the reflection and absorption of a thin film of 20nm of Bi_2O_3. The decreasing of transmittance and reflectivity simultaneously at around 3eV show that the sample starts to absorb at this range. As Bi_2O_3 is a semiconductor, we can easily deduce that this absorption is the band gap. A more refined study using the following Tauc formula [48] :

$$(\alpha h\nu)^2 = f(h\nu – E_g) \tag{3.2}$$

with α the absorbance coefficient, hν the energy and E_g the band gap, gives the band gap of Bi_2O_3 grown on Sapphire (0001) of 3.22eV as shown in figure 3.9 (c).

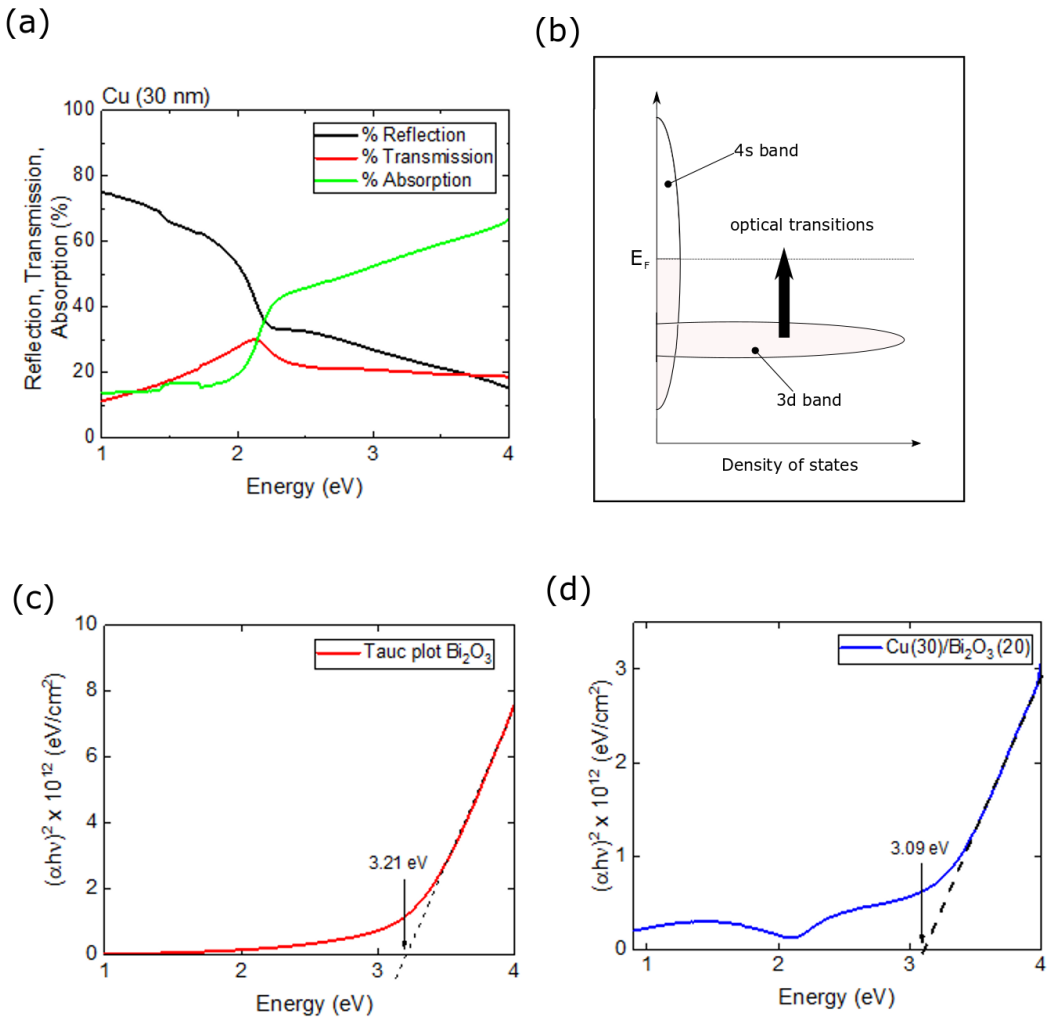

FIGURE 3.9. Optical spectroscopy of (a) Cu(30 nm) With (b) absorption mechanism explanation, (c) Tauc plot of Bi_2O_3(20 nm) grown on sapphire (0001) and (d) Tauc plot of Cu(30 nm)/Bi_2O_3(20 nm)

3.2.4.2 Thickness dependence of optical properties of Cu/Bi_2O_3

We examine the thickness dependence of optical properties of Cu/Bi_2O_3. From the measurements of reflectivity and integrated transmittance, a simple way to extract the absorption is a simple subtraction (A% = 100-T%-R%) where A% is the percentage of absorption, R the percentage of reflection and T the percentage of transmission.

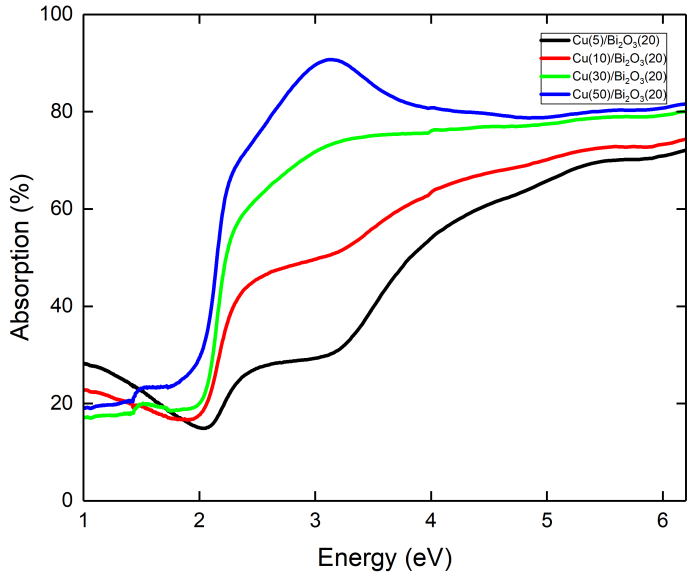

FIGURE 3.10. Absorption spectra and thickness dependence of Cu in Cu/Bi_2O_3 At low energy, the increasing of absorption supposes the existence of surface plasmon resonance in the system. At higher thicknesses, this effect is decreased due to the surface of the copper is less rough.

Figure 3.10 shows the absorption spectra and thickness dependence of Cu in Cu/Bi_2O_3 At low energy, the increasing of absorption supposes the existence of protected plasmon Schockley surface states in Cu(111) in this range. Indeed, as our samples are grown using EB-lithography, the distribution of grains of Cu is broad. AFM images in figure 3.3 confirms the existence of this distribution. At higher thicknesses, this effect is decreased due to the surface of the copper being less rough.

3.2.4.3 Optical properties comparison between Cu/Bi_2O_3 and Cu/SiO_2

Finally, we examine the optical spectroscopy of Cu/Bi_2O_3 and Cu/SiO_2. Figure 3.11 (a) shows the reflection and transmission spectra of the $Cu(10)/Bi_2O_3$ and $Cu(10)/SiO_2$. Both of them show increasing of absorption 1.90 ± 0.05 eV to 0.9 eV as explained before. Also, we can see a difference in inflection between $Cu(10)/Bi_2O_3$ and $Cu(10)/SiO_2$ around 3.1eV. This corresponds to an optical transition corresponding to Bi_2O_3 band gap. However, this band gap is slightly different from the one shown in figure 3.9 (c). A hypothesis could be that the growth of Bi_2O_3 on Cu shifts the Bi_2O_3 band gap compared to when it is grown

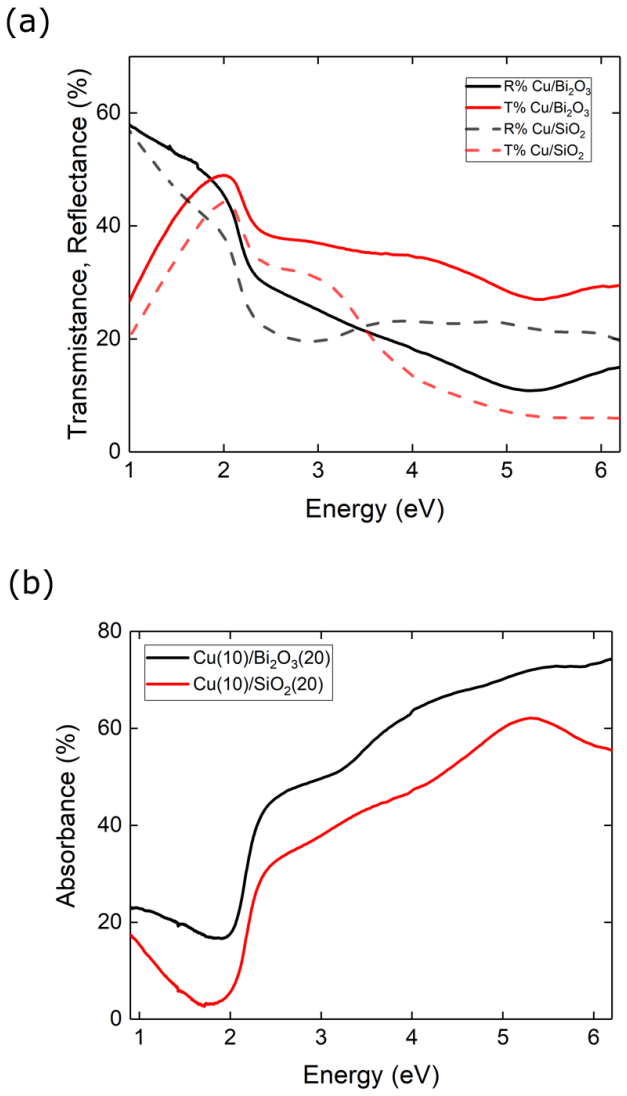

FIGURE 3.11. Spectroscopy of Cu(10 nm)/Bi_2O_3(20 nm) and Cu(10 nm)/SiO_2(20 nm). (a) shows the raw data of the diffuse transmittance or reflectance in the range from 0.8 eV to 6.2 eV of Cu(10 nm)/Bi_2O_3(20 nm) and Cu(10 nm)/SiO_2(20 nm) (b) shows the extracted absorption. Both of them show increasing of absorption from 1.90±0.05 eV to 0.9 eV.

on Sapphire(0001).

3.3 Summary

In conclusion, we explained the fabrication process of the samples that are going to be studied in the next experiments in this Thesis. We showed the step of fabrication by lithography, deposition and lift-off. We characterized the samples using Energy-Dispersive X-ray spectroscopy to confirm that only the sample contains the elements considered which is Cu, Ag and Bi. We also characterized the surface by using atomic force microscopy showing the evolution of the roughness of the Cu interfaces depending on the thickness and the creation of islands at the surface. We checked the crystallinity of the interface by X-ray diffraction at grazing incidence showing that the Copper and Silver have (111) orientation and Bi_2O_3 is in α phase. In the end, we studied the optical spectroscopy of Cu, Bi_2O_3, Cu/Bi_2O_3 and Cu/SiO_2 showing the possibility of the existence of plasmon Schockley surface states in Cu at low energy range.

CHAPTER 4

DETECTION OF SPIN ACCUMULATION USING KERR EFFECT

4.1 Introduction

As we discussed in Chapter 2, the Rashba effect describes how electrons are moving in an electric field experience a momentum dependent magnetic field. This physical phenomenon allows the generation of spin polarization from charge current better known as Edelstein effect. Recent reports showed the evidence of optical detection of in-plane spin accumulation in metallic spin Hall effect materials. In that experiment, by defocusing the laser beam O. M. J. vant Erve et. al. [49] increased the spot size of the laser to collect more spin information at the top surface and to avoid the influence of the opposite spin information from the bottom surface. In the report from C. Stamm et al. [50], researchers demonstrated the detection through MOKE with ultra high sensitivity for Kerr rotation angle down to 10^{-9} rad. However, the MOKE detection of spin accumulation in metallic systems have created skepticism, with particular concern in the influence of Joule heating generated by the injection of relatively large electrical current densities [51, 52], necessary to generate sizable spin accumulation.

This Chapter will discuss the generation of spin accumulation by injection of electrical current at the interface formed between a non-magnetic metal (Cu, Ag) and oxide (Bi_2O_3) and its optical detection by time-resolved magneto-optical Kerr effect. We will give tangi-

ble proof that this spin to charge conversion comes from the interface through Edelstein effect and is consistent with previous reports [36, 53–55]. Also different from spin Hall effect, where spin orientation is opposite at each side of the sample planes, orientation due to direct Rashba-Edelstein effect is predicted to be uniform, oriented in-plane and perpendicular to the current direction [56]. We extend our discussion to an improvement of our time-resolved transverse magneto-optical Kerr effect setup and the analysis of our estimated signals when compared with previous reports in spin Hall materials.

The content of this chapter has been published in:

Florent Auvray, Jorge Puebla, Mingran Xu, Bivas Rana, Daisuke Hashizume, Yoshichika Otani, 'Spin accumulation at nonmagnetic interface induced by direct Rashba–Edelstein effect', Journal of Materials Science: Materials in Electronics (2018)

Jorge Puebla, **Florent Auvray**, Mingran Xu, Bivas Rana, Antoine Albouy, Hanshen Tsai, Kouta Kondou, Gen Tatara, and Yoshichika Otani 'Direct optical observation of spin accumulation at nonmagnetic metal/oxide interface', Applied Physics Letters (2017)

4.2 Initial setup

For the measurement of spin accumulation supposedly created at the interface in our devices, we use a custom-made benchtop time-resolved transverse magneto-optical Kerr effect (TR-TMOKE) microscope developed by Barman et al. [57]. A description of the setup is shown in figure 4.1. Two wide bond pads with millimeter dimensions are designed at both ends of the rectangular shaped device for electrical connections. The sample stage is then placed on an x-y-z piezostage and connected with two semi-rigid coaxial cables connected to the large bond pads with the help of screws. A radio-frequency signal generator is connected to one of the semi-rigid coaxial cables for applying RF voltage across the device. Another semi-rigid coaxial cable is connected to an oscilloscope to observe the transmitted signal through the device. The laser beam is focused onto the device surface by a long working distance microscope objective with a numerical aperture of 0.14, a 5x magnification and a spot size diameter of about 3.55 μm. The incident laser beam angle is slightly shifted from the axis of the microscope objective so that the reflected beam from the sample surface can be collected by the same microscope objective through a diametrically opposite side. Moreover, we use a green LED to illuminate the

device surface with perpendicular incidence through the same microscope objective. The back-reflected light is used for real-time imaging of device and laser spot with a high spatial resolution charge coupled device (CCD) camera. CCD helps us to place the laser beam at a desired position on the device.

For the measurement of time-varying Kerr signal, a pump probe-approach. Spin accumulation signals are stroboscopically measured by locally probing sample surface by using a pulsed injection diode laser (Advanced Laser diode system PIL040) with a central wavelength of 408 nm, a pulse width of 42 ps spectral, a repetition rate of up to 1 MHz and a peak power of 1.3 mW. The RF current from the signal generator is sent to the devices and goes through a variable electronic delay generator (Colby Instruments PDL30A) that introduces a variable delay between RF current and laser pulse up to 40 ns concerning a reference time delay (we call zero-time delay). The reference time delay is decided by the internal delay of electronic devices and the length of a semi-rigid coaxial cable. The amplitude of the RF signal is modulated by 100% at a very low frequency of 20 Hz. We use an optical bridge detector and two lock-in-amplifiers to increase the signal to noise ratio of the detected signal. The role of the optical bridge detector is to minimize the change in reflectivity that is not containing any rotation due to the magnetization of the sample. The output signal of the optical bridge detector is first sent to the first lock-in-amplifiers (LIA1) whose reference signal is taken from the modulation frequency of RF signal. The output from LIA1 is then sent to the second lock-in amplifier (LIA2) whose reference signal is taken from the repetition rate of the laser beam. To measure the correct phase of time-varying sinusoidal spin accumulation signal, the signal generator is synchronized with the electronic device that triggers the laser pulses and the lock-in-amplifiers are phase locked.

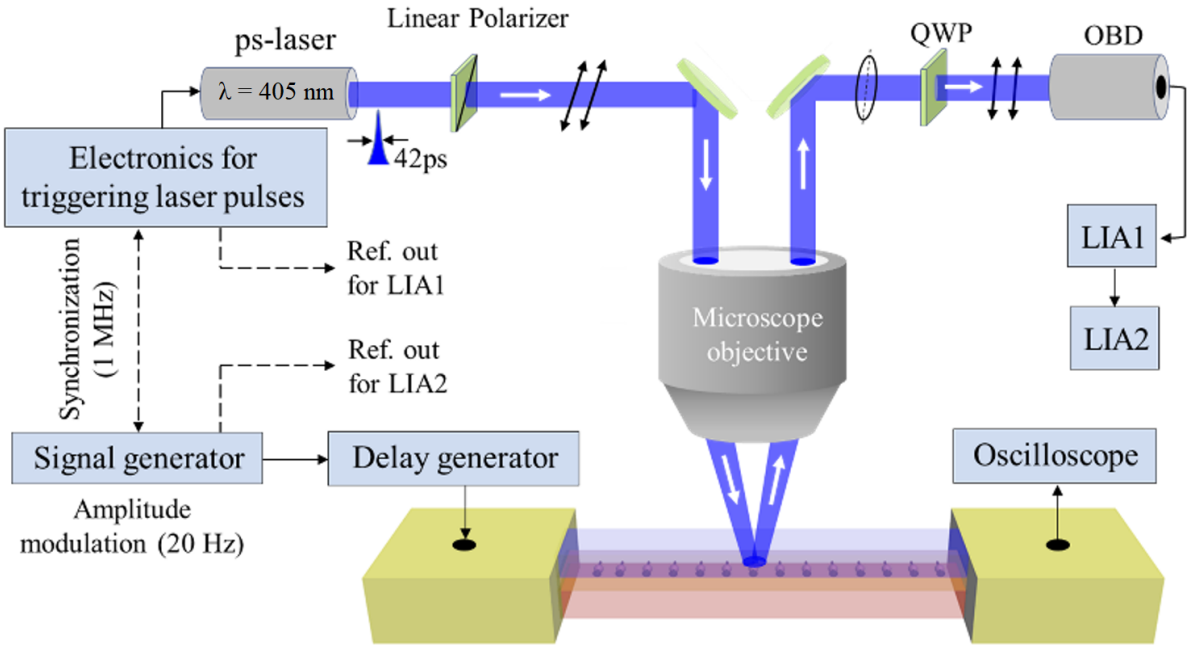

FIGURE 4.1. Experimental setup for time-resolved transverse magneto-optical Kerr effect measurements (TR-TMOKE). The incidence of light is polarized at η=45°, mixing s and p polarizations. Synchronization of two lock-ins allows measuring the time-varying in-plane component of spin polarization.

4.3 Results

4.3.1 Detection of the spin accumulation in Cu/Bi_2O_3 by Kerr rotation

Recent reports show spin to charge conversion at the Cu/Bi_2O_3 interface by spin pumping [53] and spin Seebeck effect [55]. Spin to charge conversion was also reported at the Ag/Bi interface [23] suggesting the existence of Rashba spin-orbit coupling at Ag/Bi_2O_3 interface. From these previous reports, we can indirectly infer the presence of spin accumulation on these nonmagnetic metal/oxide interfaces. We investigate the in-plane spin accumulation at the Cu/Bi_2O_3. The sample is a rectangular structure of 200μm × 600μm of Cu(20nm) and Bi_2O_3(10nm) were patterned by using UV lithography and EB-evaporation methods explained in Chapter 3 and large gold pads of 150nm thickness were added on the short edges to connect the sample to the measurement system.

The spin-orbit coupling allows generating spin accumulation by injection of electrical charge current. This is the direct Edelstein effect explained in section 2.2. For our experiments, we inject an AC sinusoidal current to our interfaces with a frequency of 100 MHz, which readily induce spin accumulation. The induced spin polarization and then the measurement of the Kerr signal should oscillate at the same periodicity as the RF signal. A schematic that shows the predicted Kerr signal depending on the RF signal is shown figure 4.2. We test the oscillating spin accumulation by our TR-TMOKE and Figure 4.3 shows one of our first experimental TR-TMOKE signals for Cu/Bi_2O_3 for a current density of 1.87×10^{12} A/m^2. There seems to have some detectable signal but the signal to noise ratio is pretty high as it can be seen in the fitting. So in the next section, we will describe how we improved the system to get a higher signal to noise ratio by using a linear polarized light with a mixed state of s- and p- polarization.

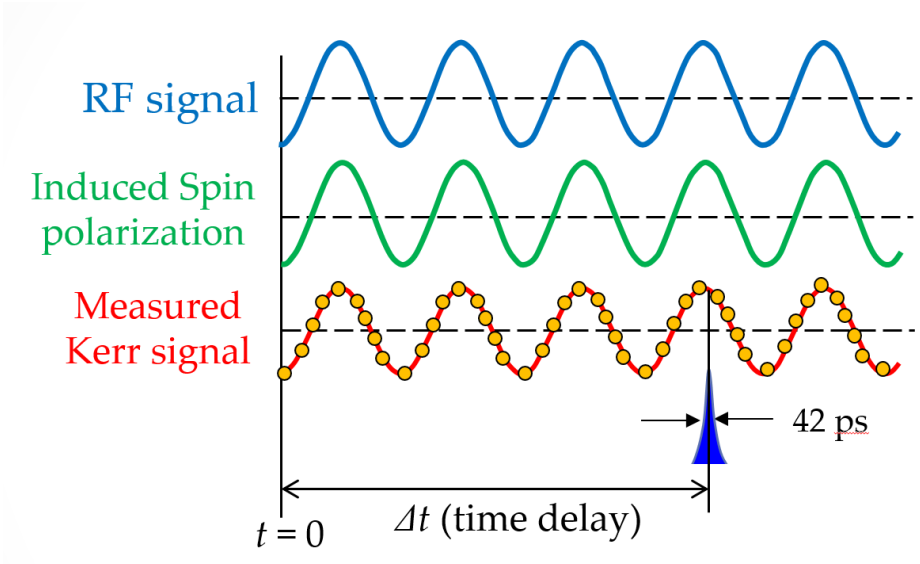

FIGURE 4.2. Description of the expected detection of spin accumulation. An injection an AC sinusoidal voltage to the interface with a certain frequency 100 MHz should readily induce spin accumulation. The induced spin polarization and then the measurement of the Kerr signal should oscillate at the same periodicity as the RF signal.

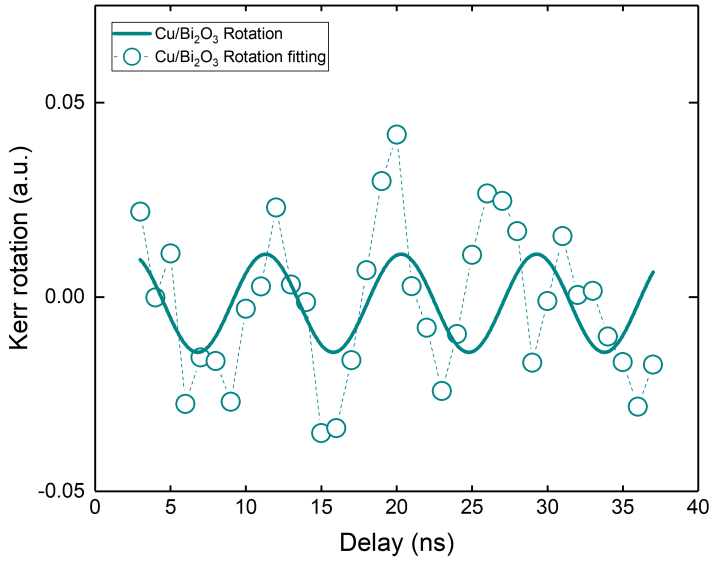

FIGURE 4.3. Kerr rotation measurement of Cu/Bi_2O_3 for 40 ns using a AC sinusoidal voltage with a frequency of 100 MHz

4.3.2 Improvement of the detection by using mixed s- and p-polarization and Kerr ellipticity measurements

To improve the sensitivities of the MOKE systems, there are two most common approaches, geometric and spectroscopic modifications. These two are based on the enhancement of the signal and the reduction of light without magnetic information. However, these strategies most likely require complicated structures. Moreover, as these structures are designed for a specific condition, these strategies can be applied only for a limited range. A more meaningful question will be to wonder if there is not a more general approach by which T-MOKE sensitivities can be enhanced.

Mixed s- p- polarization

There are some reports in which effective MOKE polarization measurements are described that achieve an enhanced signal level by mixing s- and p-polarized light in the incoming beam [44, 58, 59]. We compared the MOKE signal obtained with only p-polarization and a mixture p- and s- polarization light. The first method is the conventional direct intensity T-MOKE measurement scheme like figure in 2.16, in which

only p-polarized light a reversal of sample magnetization would cause a change of the polarization of the light. In contrast, when we set the linear polarizer at 45° to employ the mixture of p- and s- polarization light in the incidence beam, the Kerr signal is enhanced. This method has been tested in [44, 59].

Comparison of Kerr rotation and Kerr ellipticity signals

As another way to enhance the detectability, it has been shown that Rashba systems can own a strong dichroism and that dichroism enhances the Kerr ellipticity [60, 61]. As we expect a strong Rashba effect at the interface of Cu/Bi_2O_3, the Kerr ellipticity of the Rashba interface may be stronger than Kerr rotation. So, by using a quarter wave plate to collect Kerr ellipticity instead of Kerr rotation, the signal could be enhanced. A comparison of Kerr rotation and Kerr ellipticity is observed in figure 4.4. We can see a strong enhancement of the signal to noise ratio in Kerr ellipticity compared to Kerr rotation. As a consequence, the next results that will be shown in this Chapter will use display Kerr ellipticity measurements.

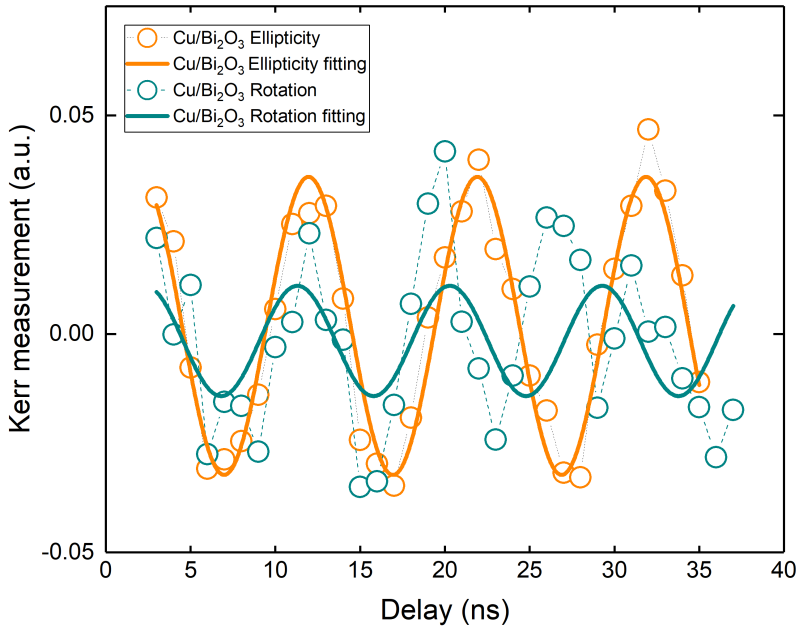

FIGURE 4.4. Comparison between Kerr rotation and Kerr ellipticity signals of Cu/Bi_2O_3

4.3.3 Comparison of Kerr ellipticity signal between Cu/Bi_2O_3 and Cu/Al_2O_3

We performed measurements for $Cu(20nm)/Al_2O_3(10nm)$. This is shown in figure 4.5. Orange points represent the Cu/Bi_2O_3 Kerr ellipticity signal and Green triangle points represent the Cu/Al_2O_3 Kerr ellipticity measurement. Compared to Cu/Bi_2O_3, Cu/Al_2O_3 does not have any periodicity. We attribute that to the fact that Cu/Al_2O_3 that the spin accumulation created at the interface is too small to be detected, giving erratic signal.

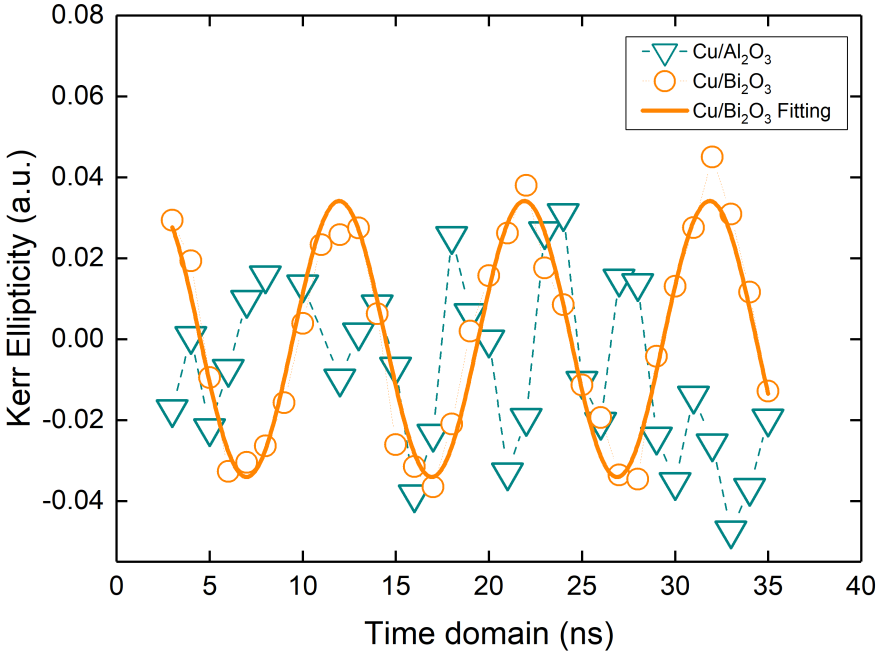

FIGURE 4.5. Comparison of Kerr ellipticity signals between reference sample Cu/Al_2O_3 (grey) and Cu/Bi_2O_3 (orange)

4.3.4 Comparison of Kerr ellipticity signal between Cu/Bi_2O_3 and Ag/Bi_2O_3

We performed measurements for Ag/Bi_2O_3 samples with similar shapes and thicknesses as Cu/Bi_2O_3. The result is shown in figure 4.6. Orange curve represents the Cu/Bi_2O_3 Kerr ellipticity signal while grey curve represents the Ag/Bi_2O_3 Kerr ellipticity. From fitting (solid lines) of figure 4.6, we can extract a time periodicity of our oscillating signal of 10 ns or 100 MHz in a frequency domain, correlated to the frequency of our AC voltage excitation.

4.3.5 Position dependence of Ag/Bi_2O_3 and Cu/Bi_2O_3

Moreover, spatially uniform spin accumulation is also expected to originate from a flow of electric current on Rashba type interfaces. So, we scanned the position of our laser spot along the Cu/Bi_2O_3 and Ag/Bi_2O_3 interfaces and examined the relative change in amplitude of TR-TMOKE signal. Figures 4.7 and 4.8 show the comparison of the obtained

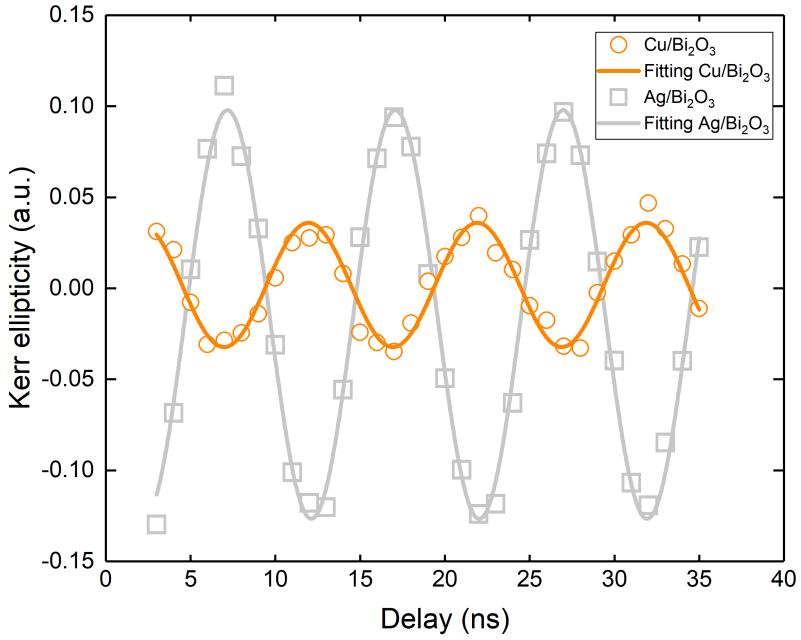

FIGURE 4.6. Comparaison between MOKE signals of Cu/Bi_2O_3 and Ag/Bi_2O_3

TR-TMOKE signal for three different laser spot positions along the interfaces parallel to the electrical charge flow. As a reminder, the full area of our sample is 200 μm × 600 μm and the nominal laser spot diameter is about 3.55 μm.

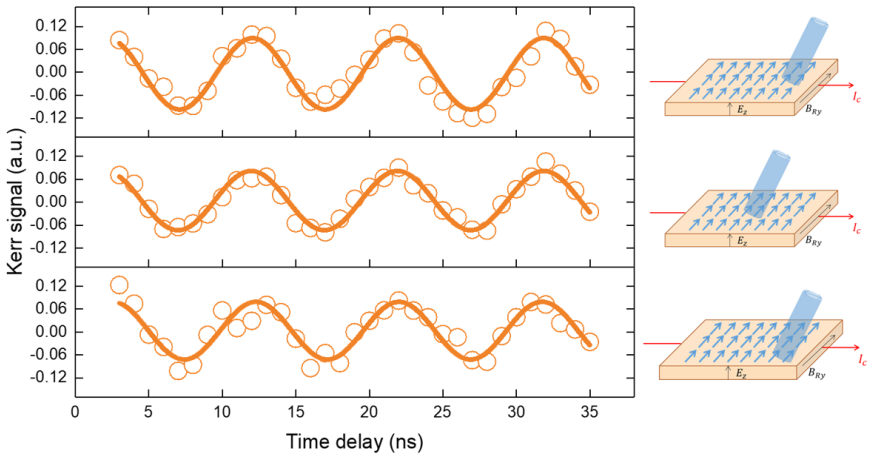

FIGURE 4.7. Kerr ellipticity depending on the position in Cu/Bi_2O_3

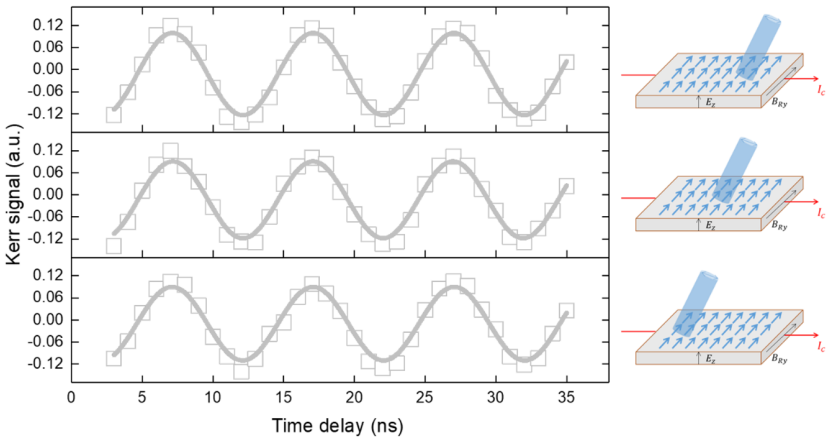

FIGURE 4.8. Kerr ellipticity depending on the position in Ag/Bi_2O_3

4.4 Discussion

4.4.1 Comparison of generation of spin accumulation by spin Hall effect mechanism and by Edelstein effect mechanism.

In this subsection, we discuss the differences between the generation of spin accumulation by spin Hall effect and Edelstein effect and their optical detection. Intrinsically, spin accumulation generated by bulk spin Hall effect and direct Edelstein effect at interfaces have different distribution of spin orientations. Spin polarization via bulk spin Hall effect is oriented perpendicular to the electron flow on all the four planes which are transverse to the charge current as shown in figure 4.9 (a). In contrast, spin accumulation via Edelstein effect at interfaces is in-plane, homogeneous and perpendicular to the electron flow direction like in figure 4.9 (b). These configurations of spin accumulation are important facts when we try to detect in-plane spin accumulation by optical Kerr effects. For example, if the penetration depth of a given laser in a MOKE setup is larger than half of the thickness of sample displaying spin Hall effect, photons interact spin with two spin orientation components related to each half of the sample which result in a reduction of the total signal detected as the spins up and down will compensate each other. One way to minimize this issue is to reduce the interaction with the polarized electrons at the bottom surface by defocusing the laser beam and at the same time it increases the collection area at the sample top surface as done by O. M. J. vant Erve et. al. [49] in their optical detection of spin Hall effect in Pt and W. However, similar issue is

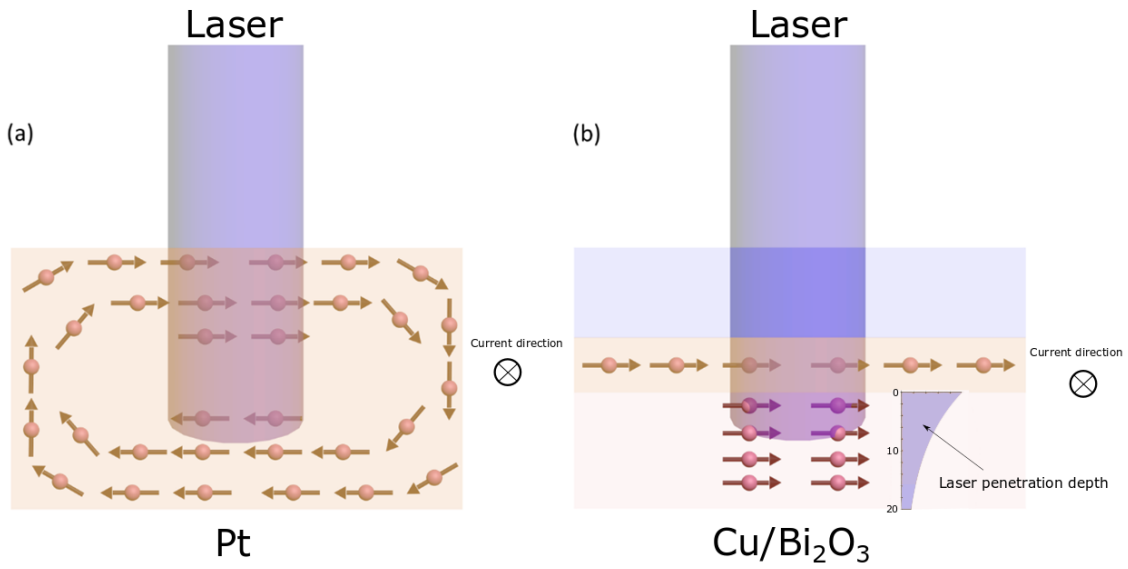

FIGURE 4.9. Comparison of generation of spin accumulation by (a) spin Hall effect mechanism and (b) by Edelstein effect mechanism.

not present at Rashba interfaces where the spin accumulation can be enhanced by the coherent tunneling of spins from the interface into the nonmagnetic metal bulk. In the experiments, the spin accumulation is generated at the Cu/Bi_2O_3 and Ag/Bi_2O_3 interface and it is possible for these spins to diffuse into the metal with a certain probability[54]. Indeed, If the spin tunneling occurs and the spin diffusion length is larger than the thickness of nonmagnetic metal layers, the detected spin accumulation will be increased with the penetration depth of the laser. Recent experiments of spin magneto-resistance at the Cu/Bi_2O_3 interface observed a diffusion of accumulated spins of 33.9% from the interface into the bulk Cu [54]. These characteristics indicate that the density of spins detected in our experiments is enhanced by the diffused spins into the bulk, with a detection limit set by the penetration depth of our laser.

4.4.2 Charge to spin conversion and sign difference between Cu/Bi_2O_3 and Ag/Bi_2O_3

A comparison between Cu/Bi_2O_3 and Ag/Bi_2O_3 signals is shown in figure 4.6. From this figure, we can observe that Kerr ellipticity detected signals for Cu/Bi_2O_3 and Ag/Bi_2O_3

have opposite phases which implies these two systems have opposite orientation of spin accumulation. The orientation of spin polarization and the corresponding spin accumulation are directly dependent on the amplitude of Rashba parameter and the sign of effective mass m_e^*, which determines the splitting order of inner and outer energy branches [62] as explained in section 2.2. Previous spin pumping experiments estimated α_R for Cu/Bi_2O_3 and Ag/Bi_2O_3 [53] (shown in table 4.1) and the sign of effective mass m is negative for both interfaces. Indeed, Cu and Ag by themselves are conductors with parabolic bands; however, when forming a Rashba interface in contact with Bi_2O_3 the electrons take on the new paradigm of internal forces due to the new periodic potential. The negative mass describes that the electrons respond to these forces in opposite direction to what a free electron would do. This can be observed when testing the curvature of the dispersion curve. We take experimental reports that show the dispersion curves for Cu/Bi [62] and Ag/Bi [23] as an approximation. Finally, from our position dependence measurements figures 4.7 and 4.8, we can observe that the amplitude of the TR-TMOKE signal is constant along the Cu/Bi_2O_3 and Ag/Bi_2O_3 interface reflecting spatially homogeneous spin accumulation, and inferring negligible influence of heat gradients in our measurements, giving another proof that our signal comes from charge to spin conversion through Edelstein effect.

4.4.3 Relative amplitude of expected spin accumulation

Now, we discuss about the relative amplitude of our TR-TMOKE signals and the expected spin accumulation. The 3D density of spins at the interface is related to the electrical charge current density through the Rashba parameter α_R, as follows [56] :

$$< \delta S >= \frac{m_e^* \alpha_R}{e\hbar\epsilon_F} J_{cx} \tag{4.1}$$

where ϵ_F is the Fermi energy, which are taken from the nonmagnetic metal values for Cu and Ag, and m_e^* is the effective mass, which is approximated to the mass of a free electron at our interfaces and J_{cx} the electrical current density. For our estimation, we assign an interface thickness of one atomic lattice t=0.4 nm [23, 36]. All the parameters are summarized in table 4.1.

It gives an expected of spin accumulation <δS> of 14.0 μeV for Cu/Bi_2O_3 and 23.7 μeV for Ag/Bi_2O_3. By assuming that the spin accumulation created at the interface diffuses in the bulk, and the spin diffusion lengths at room temperature for Cu [63] and Ag [10]

	ϵ_F (eV)	m_e^* (10^{-31} kg)	α_R (eV Å)	J_{cx} (10^{12} A/m^2)
Cu/Bi_2O_3	7	9.11	-0.256±0.03	1.87
Ag/Bi_2O_3	5.5	9.11	0.186±0.04	2.16

TABLE 4.1. Relevant parameters for estimation of spin accumulation in Cu/Bi_2O_3 and Ag/Bi_2O_3

are much longer than our layer thickness (20 nm), the detected spin accumulation would depend mainly in the penetration depth of our laser into the metal layers which is about 11 nm for both samples and the extinction ratio for both metals (Cu, Ag) are very similar at our laser wavelength (408 nm) [64].

By a simple integration on the metal thickness :

$$\int_0^{20} e^{-\frac{x}{11}} dx = 9.3$$

We find an enhancement of the signal by a factor of 9.3 in our samples. The spin accumulation expected at the interface of Cu/Bi_2O_3 is 14.0 μeV and at the interface of Ag/Bi_2O_3 is 23.7μeV. It gives a estimation of the detected spin accumulation by our system of 130.2 μeV for Cu/Bi_2O_3 and 220.4 μeV for Ag/Bi_2O_3. Finally, We compare the ratio between TR-TMOKE signal amplitudes for Cu/Bi_2O_3 and Ag/Bi_2O_3 and the ratio of their total spin accumulations. The amplitudes of our signals have been normalized by the corresponding reflectivity for Cu/Bi_2O_3 and Ag/Bi_2O_3 at our laser wavelength (408 nm) [64]. From our fittings in figure 4.6, we obtain peak amplitudes of 0.077 and 0.112 for Cu/Bi_2O_3 and Ag/Bi_2O_3, giving a ratio of 1.45, which is in a good agreement with the ratio of their estimated spin accumulation equal to 1.69. For our estimations, we assume that spin Hall effect is negligible at our samples, as it has been tested previously by spin pumping measurements for Py/Cu and Py/Bi_2O_3 bilayers [36].

4.5 Summary

We observed the homogeneous in-plane current induced spin accumulation at room temperature due to Rashba-like spin-orbit coupling at the nonmagnetic metal/oxide interface by TR-TMOKE. Opposite phases of Kerr ellipticity signals for Cu/Bi_2O_3 and Ag/Bi_2O_3 interfaces correspond to their intrinsic opposite spin configurations, independently determined by spin pumping measurements[53]. The absence of a quantitative signal on Cu/Al_2O_3 that does not have spin-orbit interaction at the interface also gives another

indication that signal comes from the Rashba-like spin-orbit coupling. Both interfaces tested at three different laser spot positions along the interface parallel to the electrical charge flow give respectively the same signals and comparison between peak to peak signals and expected spin accumulation of the systems show good agreement, proving the validity of the values of their Rashba parameter α_R by characterization method without external magnetic field or proximity to ferromagnetic layers. The results also show the feasibility of characterizing the spin accumulation by Kerr effect magnetometry [49, 50]. We further discussed the estimation of our spin accumulation and compare our results with previous reports of MOKE detection of spin accumulation in SHE materials [49, 50].

At the end, the observation of spin accumulation is the result of the efficient generation of spin accumulation by direct Edelstein effect at our interfaces [23, 36, 56] and the high sensitivity of our experimental setup, which combines sine current modulation and lock-in detection techniques, strongly minimizing the spurious asymmetries of the detected signals [50] with the addition of the balanced mix of the s- and p-polarizations of the incident light in transverse geometry, which enhance the signal to noise ratio of the detected Kerr signals compared with standard MOKE configurations [44, 58, 59].

CHAPTER 5

HELICITY DEPENDENT PHOTOVOLTAIC CONVERSION AT NONMAGNETIC INTERFACE WITH SPATIAL INVERSION ASYMMETRY

5.1 Introduction

In the previous chapter, we showed the detection of spin accumulation at the interface of non-magnetic metal/oxide by using TR-MOKE system. Now, we move on the study of the helicity dependence and photovoltaic conversion at this interface. Photovoltaic conversion with helicity dependence in previous reports arises from charge separation due to internal build-in voltage in p-n junctions or inverse spin Hall effect [16, 18, 65]. At the Cu/Bi_2O_3 interface the spatial inversion asymmetry induces spin-orbit coupling leading to the conversion of spin current to charge current known as inverse Edelstein effect as described Chapter 3.

It can be suggested that information from light polarization can be transformed into an electric signal by combining the optical selection rules and the inverse Edelstein effect. In this chapter, we will show the helicity dependent photovoltaic generation at the Cu/Bi_2O_3 interface at room temperature, where carriers are excited by monochromatic light across the optical transition of Bi_2O_3 or via hot electrons induced by the plasmon surface states in Cu.

The content of this chapter is still on going at the time of writing this thesis.

5.2 Experimental Setup

We present here the setup used in our experiment as shown in figure 5.1. The laser beam has an incidence angle θ and an azimuthal angle of ψ shown in figure 5.2 (a). Our light excitation is continuous wave lasers at energies of 1.16 eV, 1.96 eV, and 3.05 eV. The laser spots are adjusted to approximately 400 μm with a Gaussian profile for all the lasers, and place at the center of our sample surface to minimize temperature gradients. The photon polarization is controlled by a linear polarizer and a quarter wave plate mounted on a mechanical rotator. The voltage is detected by a lock-in amplifier in an open circuit mode synced at 400 Hz with a mechanical chopper.

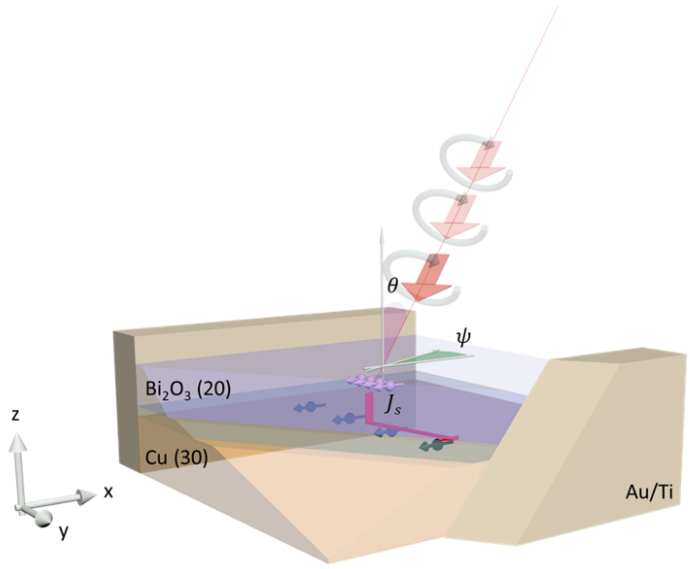

FIGURE 5.1. Schematic illustration of the experimental setup. The schematic shows the laser that illuminates the sample at an incidence angle θ and an azimuthal angle ψ with polarization $\sigma^{\pm}$.

5.3 Evaluation of the helicity dependent of photovoltaic conversion

We investigate optical spin to charge conversion at Cu/Bi_2O_3 heterostructure. Similarly to the previous experiment, the sample is a rectangular structure of 1.5 mm × 900 μm of

Cu(30 nm) and Bi_2O_3(20 nm) were made in using UV lithography and EB-evaporation methods explained in Chapter 3 and large gold pads of 150nm thickness were added on the short edges to connect the sample to the measurement system.
The spin-orbit coupling allows to generate charge voltage by injection of optical spin by using circularly polarized light, similar to inverse Edelstein effect explained section in 2.2. For our experiments, we inject a polarized light to our heterostructure and collect the voltage changes of the sample while changing the polarization of the light. The induced charge voltage should phase at the same periodicity as the change of light polarization. We first test the change of voltage at the center of our heterostructure by putting the laser in the center with an energy of 1.96 eV. The results are shown in figure 5.2. We can see in this figure that changing contributions of polarized light due to the rotation of the quarter wave plate angle φ leads to a periodic modulation in photovoltage with a periodicity of 90°.
Photovoltage peaks have different amplitudes, showing periodically two different values. This asymmetry comes from the circularly polarized light modulation. To better describe the contributions in our modulated signal, we fit the data with the following phenomenological formula :

$$V_{out} = V_C \sin(2\varphi) + L_1 \sin(4\varphi) + L_2 \cos(4\varphi) + A \tag{5.1}$$

Here, V_C represents the amplitude associated with the degree of circular polarization of light or helicity which is the solid red line in figure 5.2, L_1 is the amplitude associated with the linear polarization of light represented by the blue dash line in figure 5.2, L_2 depends on the Fresnel coefficients represented by green dash line in figure 5.2, and A is a none modulated photovoltage offset.

5.4 Study of the photovoltage generation by Cu/Bi_2O_3 with a laser energy of 3.05ev

5.4.1 Oblique incidence dependence at 3.05 eV

We performed measurements oblique incidence θ for Cu/Bi_2O_3 samples at room temperature for laser energy of 3.05eV at 1mW laser power. The result of the incidence angle dependence of the circular photovoltage V_c is presented figure 5.3. The blue curve of

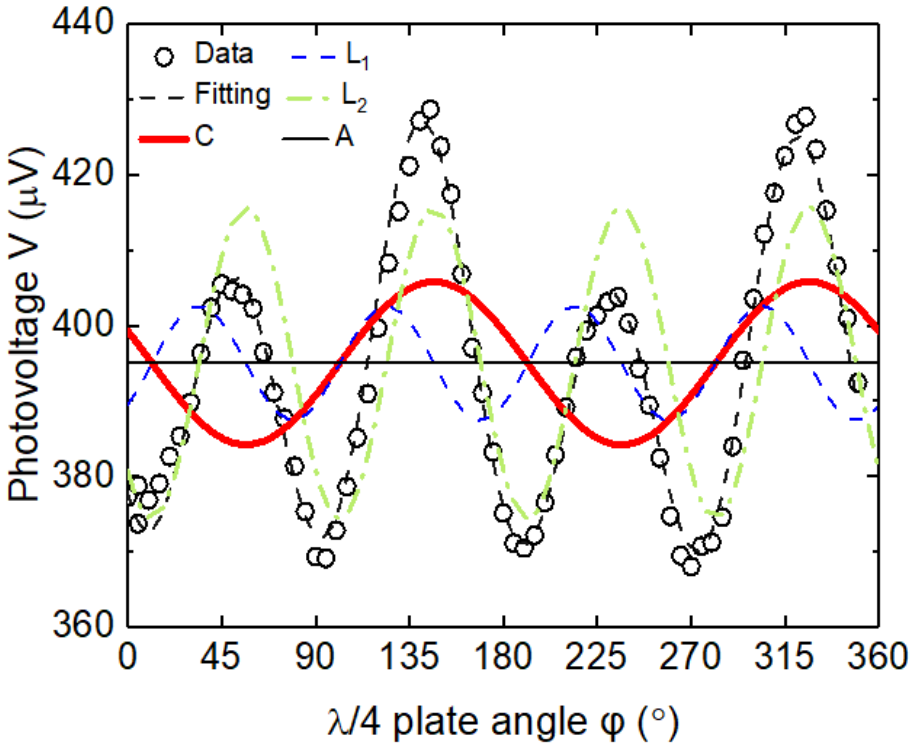

FIGURE 5.2. Photovoltage measurement at room temperature as a function of the phase angle φ under 70° incidence when the plot light is in the middle. The dashed line (black) is the fitting using equation 5.1, The dotted lines (green and blue) and the red line are the respectively the linear dependence and circular dependence. The black line indicates the background voltage A.

figure 5.3 shows the fitting that will be explained next section. The voltage detected has a maximum of 3.10±0.40 μV at θ=50°

5.4.2 Discussion of origin of the helicity dependence at a laser energy of 3.05eV

By exciting our sample with a laser energy of 3.05 eV, valence band electrons are excited to the conduction band of Bi_2O_3. We show in the optical spectroscopy characterization of the Cu/Bi_2O_3 that Bi_2O_3 has a band gap around 3.13 eV in figure 3.9. So, following Weber et al. [66], we can fit the incidence angle θ dependence of the circularly polarized

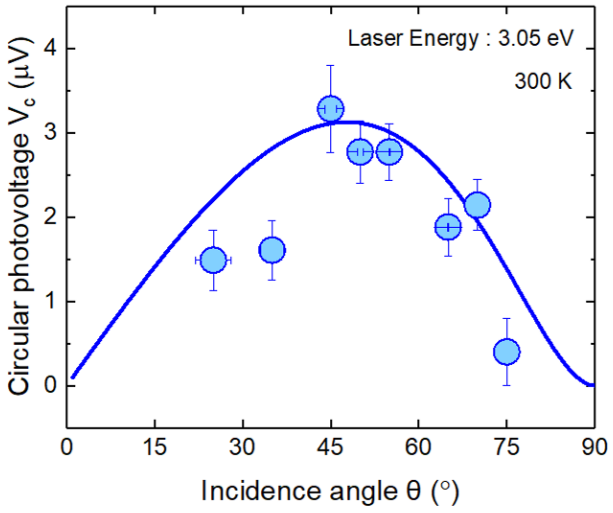

FIGURE 5.3. Oblique incidence dependence. Photon energy of 3.05 eV excites spin polarized electrons across the Bi_2O_3 band gap. Rounds show the circularly polarized voltage V_C at oblique incidence angles θ.

voltage by

$$V_C = t_s(\theta)t_p(\theta)\sin(\theta) \tag{5.2}$$

where t_s and t_p are the transmission coefficient of the s(p) polarized light that can be written :

$$t_s t_p = \frac{4\cos^2\theta}{\left(\cos\theta + \sqrt{n^2_{Bi_2O_3} - \sin^2\theta}\right)\left(n^2_{Bi_2O_3}\cos\theta + \sqrt{n^2_{Bi_2O_3} - sin^2\theta}\right)}$$

with $n_{Bi_2O_3}$= 2.3 the refractive index is taken from Condurache-Bota et al. [67]. The maximum absolute value of the voltage created by the circularly polarized light for a laser power of 1mW and an incidence angle θ = 50° is 3.1±0.4 V, which is comparable to previous reports obtained by spin Hall effect conversion [16] that uses a laser poser of 10 mW.

Two main factors contribute to the oblique incidence dependence: i) the degree of circular polarization, ii) and the angle dependence between spin polarization vector

(σ_s) and spin current (J_s), such that $V_C \propto \sigma_s \times J_s$. The degree of circular polarization depends on the absorption of s-polarised component and p-polarized component, which is unaffected at normal incidence. (θ = 0°) and decreases significantly at higher angles. While, $\sigma_s \times J_s$ is negligible at normal incidence (θ = 0°) and gradually increases towards maximum at grazing angles. As a result, for excitation energy above the Bi_2O_3 band gap, a minimum of V_C is located at θ = 0°, and maximum at θ = 50°, similar to previous reports for Pt/GaAs [16].

5.4.3 Extraction of the spin current from the signal

From the fitting, we can extract the amplitude of the photovoltage V_{out}, which depends exclusively on the helicity of light, V_C. We estimate roughly the optically generated spin current by

$$J_s = \frac{V_C}{\lambda_{IEE} w R} \tag{5.3}$$

Where λ_{IEE} is the inverse Edelstein length, a the width of our interface and R the sample resistance.
The spin current by taking the voltage due to circular polarization from fitting at Figure, V_C = 3.1 10^{-6} V, λ_{IEE}=1.70 10^{-10} m, ω = 0.9 10^{-3} m and R=4.8 Ω , we obtain $J_s = 4\times10^6$ A/m^2 with a laser power of 1 mW, which is comparable with the spin current commonly generated by spin pumping experiments [53] but better than previous reports of circular photovoltaic conversion by inverse spin Hall effect [16, 18] that used a laser of 10 mW at λ = 670 nm.

5.5 Influence of the photovoltage generated by Cu/Bi_2O_3 by a laser energy 1.96ev

5.5.1 Oblique incidence dependence at 1.96 eV

Now, we present the dependence of the circularly polarized voltage V_C with the angle of incidence, for laser energy of 1.96 eV at 1.5 mW laser power. The voltage detected has a maximum of 15±0.1 V at θ=70°. In contrast to previous experiments, the energy of the laser does not excite the direct optical transition of Bi_2O_3. Since the preservation of angular momentum via selection rules require electronic optical transitions, the circularly

polarized voltage V_C generated by 1.96 eV laser is somehow unexpected.

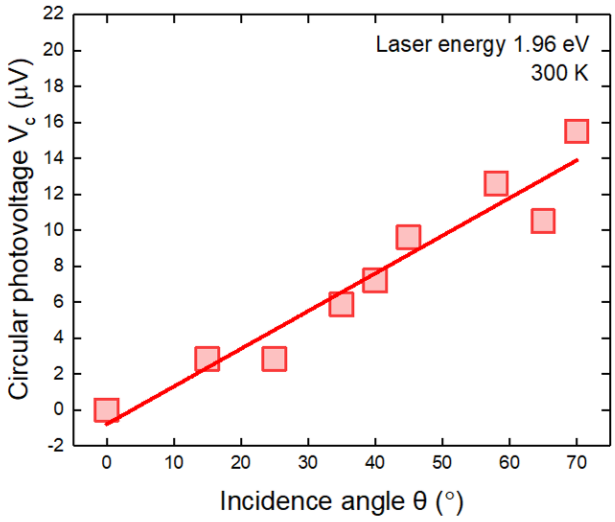

FIGURE 5.4. Oblique incidence dependence of the circularly polarized photovoltage at a photon energy of 1.96 eV. Open squares show the circularly polarized voltage V_C at oblique incidence angles.

5.5.2 Voltage signal comparison between laser at 1.96 eV and 1.16 eV

Then, we compare the circularl photovoltage V_C generated by 1.96 eV and 1.16 eV energy lasers, at θ = 70° and ψ = 0° . Figure 5.5 shows that V_C (1.96eV) $\gg$ V_C (1.16eV), indicating that the threshold to detect photovoltage coming from the circular polarization of light is between 1.16eV and 1.96 eV, and also showing negligible contribution of circular polarized photovoltage coming from Si substrate, which has a band gap of 1.1 eV.

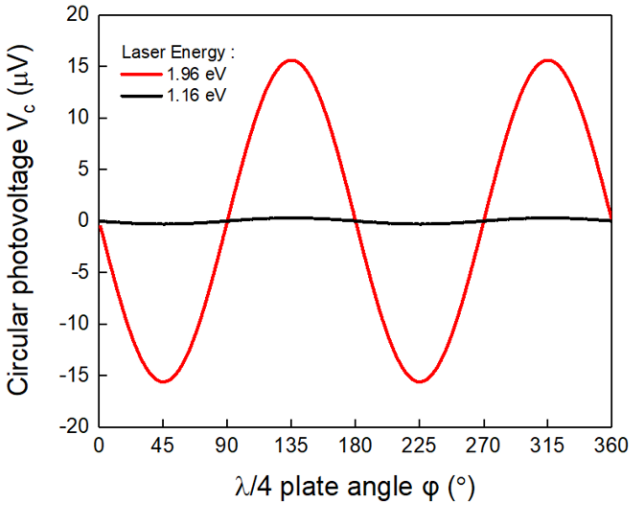

FIGURE 5.5. Compare the circularly photovoltage V_C generated by 1.96 eV and 1.16 eV energy lasers, at θ = 70° and ψ = 0°.

5.5.3 Voltage signal comparison between laser at between Cu and Cu/Bi_2O_3

We also compare the photovoltage generated at 1.96 eV by Cu and Cu/Bi_2O_3, at θ = 70° and ψ= 0°. Figure 5.6 shows that there is no photovoltage induced by circularly polarized light, indicating the importance of the presence of the interface between Cu and Bi_2O_3 to generate photovoltage from circularly polarized light. We think that the small phase shift between Cu and Cu/Bi_2O_3 is due to a misalignment of the quarter wave plate during the measurements.

5.5.4 Hypothesis related to the origin of the helicity dependent photovoltage with excitation of 1.96 eV

Absorption spectroscopy measurements show a plasmonic like absorption spectra at an energy E_{pl} = 1.9 eV in section 3.3.3. Similar plasmonic like absorption was observed for Cu and Ag protected by graphene [68]. Photovoltaic and photocatalytic devices based on

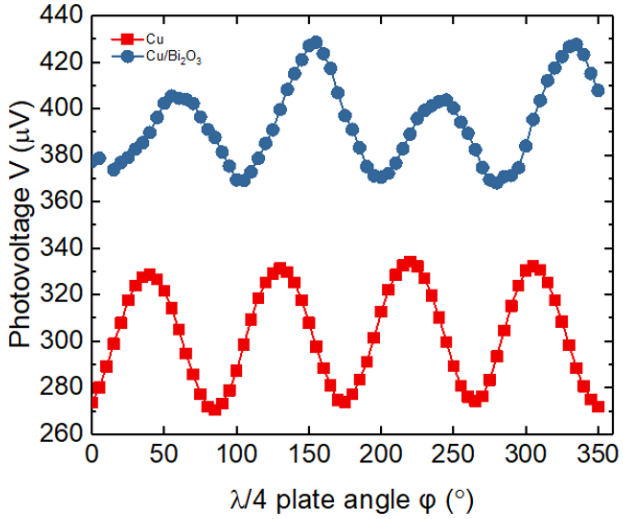

FIGURE 5.6. Comparison the photovoltage V_{out} of Cu and Cu/Bi_2O_3 generated with a laser at an energy of 1.96 eV, 1.5mW, at θ = 70° and ψ = 0°.

plasmon induced hot electrons at metal nanoparticles/metal oxide interfaces have also been reported recently, holding a promise for large conversion efficiencies [69, 70]. At this interval of energies two other scenarios may also arise: i) gap states at our Cu/Bi_2O_3 interface where the theory is explained chapter 2 and ii) hybridization of Cu and oxygen atoms at the interface.

5.5.4.1 Possibility of metal-induced gap states in Cu/Bi_2O_3 interface

At metal/semiconductor (or insulator) interface, the electron wavefunction of the metallic side penetrates into the forbidden gap creating the so-called metal-induced gap states (MIGS). The MIGS have been studied extensively before [71–73] as we talked about it in section 2.1.4, and are determining for the characteristics of the metal-semiconductor junctions such as the pinning effect [74]. Also, recently a new mechanism of Fermi level pinning is being discussed to arise from two interface behaviors: metal work function modification by interface dipole formation due to charge transfer, and appearance of gap

states due interface hybridization [75]. This mechanism is different from well-known MIGS and can result in the formation of Ohmic junctions with gap states. Because of the lack of circular photovoltage in Cu/Bi_2O_3 at 1.16 eV in figure 5.5, we can assume that there is no MIGS. However, with our actual data, we are not able to totally rule out the possibility of MIGS between 1.16 and 1.96 eV. However, preliminary results with first principle analysis of Cu/Bi_2O_3 (shown in conclusion later), also did not show any MIGS.

5.5.4.2 Hybridization of Cu and Oxygen atoms at the interface

Another possibility is that Cu and O have respectively $3p^6$, $3d^{10}$, $4p^1$ and $2p^2$, $2p^4$ as valence states electrons which would create CuO, Cu_2O or Cu_4O_3 oxide compounds. These oxides are p-type semiconductors with a band gap included between 1 eV and 2.6 eV, energies within the interval of our photovoltage excitation. However, grazing XRD spectroscopy and optical absorption measurements did not show evidence of any other oxides or materials rather than Cu and Bi_2O_3.

5.5.4.3 Metal/oxide protected plasmon Schockley surface states

It is possible to assume that the photovoltaic conversion to the metal oxide protected plasmon Schockley surface states in Cu(111) based on our absorption characterization and previous analysis of other scenarios. Photon-plasmon absorption can decay via [76]: radiative transition, nonradiative transition, resonant energy transfer and uphill electron transfer to a semiconductor in direct contact. The electron transfer occurs when a hot electron is generated and acquired energy enough to overcome the metal/semiconductor barrier [70]. If the hot electron is generated via photoelectric effect through Landau damping, significant losses of energy and angular momentum may occur [77]; however, if the hot electron is generated and directly excited to the conduction band of the semiconductor energy and angular momentum losses are reduced. This process is better known as photoinduced interfacial electron transition[76, 77]. For facilitating the latter process, interfacial charge transfer and low energy Schottky barrier should be present. At our Cu/Bi_2O_3 interface, we have a low energy Schottky barrier reflected in our I-V characterization.

As said in the previous section, the degree of circular polarization, angle dependence between the spin polarization vector (σ_s) and spin current (J_s) leads to the oblique incidence dependence. For excitation energy below the Bi_2O_3 band gap (1.96 eV), the photons are not absorbed in the Bi_2O_3 and making the degree of circular polarization

negligibly accepted by the incidence angle, showing just oblique incidence dependence on J_s in figure 5.4. At this energy (1.96 eV) plasmon induced hot electrons acquired and preserved the light-induced polarisation and are converted to charge current via the IEE at the Cu/Bi_2O_3 interface. A possibility could be that a strong hybridization of Cu-O-Bi charge states at our interface and Rashba splitting, allowing the plasmon-induced charge separation mechanism and IEE spin to charge conversion. Transverse photovoltage induced by circularly polarized light can also be generated in surface state polaritons via an asymmetric variation of the photon drag effect [78]. This mechanism requires only surface state plasmons in metals and not necessarily the assistance of a semiconductor such as a plasmon induced hot electrons mechanism [70, 76]. However, we tested the response of a Cu layer to circularly polarized light at 1.96 eV as shown in figure 5.6. While the Cu preserved the optical absorption due to Schockley surface states, We cannot see significant transverse photovoltage related to circularly polarized light. Therefore, furthering suggesting the combination of plasmon-induced hot electrons and IEE as the origin for our circular polarized photovoltage at the Cu/Bi_2O_3 interface.

5.6 Summary

We showed the photovoltaic conversion with helicity dependence at Cu/Bi_2O_3 interface at visible energies where solar spectrum peaks. Due to the increasing number of interfaces with broken spatial symmetry, we expect that the present work motivates further studies, advancing conversion efficiencies and further understanding towards spin orbitronics in photovoltaics. From our present and previous reports, we have the indication of spin to charge conversion at Cu/Bi_2O_3 interface due to Rashba spin-orbit coupling. Rashba spin-orbit coupling is suggested as a key component to suppress carrier recombination and enhanced carrier lifetime in perovskites. Moreover, we observed an efficient photovoltaic conversion arising from a plasmonic like absorption at our Cu/Bi_2O_3 interface.

CHAPTER 6

CONCLUSIONS AND FUTURE WORK

6.1 Conclusion

To conclude, we studied the effects of optical spin-charge interconversion at the non-magnetic metal/oxide interfaces. Especially, we are able to characterize the spin accumulation at Cu/Bi_2O_3 and Ag/Bi_2O_3 interfaces and show that these interfaces have opposite spin momentum configurations. Also, we show that circularly polarized light with an energy near the band gap of Bi_2O_3 can be converted into charge current in Cu//Bi_2O_3 interface. More surprisingly, we show the existence of helicity dependent photovoltage at energy range close to the plasmon resonance of copper. Also, the result from optical spectroscopy shows plasmonic like absorption at Cu/Bi_2O_3 interface. Based these two facts, we hypothesize a new mechanism for photovoltage generation that relies on plasmon resonance and Rashba interfaces. To sum up, we demonstrate that plasmonic energy conversion holds the promise for efficient mechanism of electron-hole separation in photovoltaic devices at low costs. Moreover, the study reflects the relevance of selecting appropriate engineering of heterojunctions. Furthermore, considering the increase interest of systems with spatial inversion asymmetry, we expect that the presented work would motivate further studies on advancing conversion efficiencies and further understanding towards spintronics in photovoltaics.

6.2 Future works

Through all this thesis, we obtained experimental evidence by diverse methods of spin to charge interconversion phenomena link to spin-orbit interaction at the interface between non-magnetic metal (Cu,Ag) and Bi_2O_3. However, these diverse experimental pieces of evidence of spin-charge interconversion due to spin-orbit coupling at are not a direct characterization of the 2DEG formed at our interfaces. Usually, characterization of interfaces or surfaces with spin-orbit coupling is achieved by angle-resolved photoemission spectroscopy. This characterization technique requires high quality of crystalline structures. However, the interfaces are formed by polymorphous layers with a low crystalline quality, which makes impossible the characterization by angle-resolved photoemission spectroscopy.

We present here some future preliminary results of experiments and simulations that are related to the results obtained in the present thesis. Especially, we show the possible characterization of the electron gas at the interface by ellipsometry and simulation of the band structure of Cu/Bi_2O_3 at 1.98 eV above the Fermi level, to enforce the hypothesis of novel mechanism made in this thesis.

6.2.1 Ellipsometry characterization of interfacial two-dimensional electron gas and spin orbit coupling

A possible way to characterize of the interfaces would be by angle-resolved spectroscopic ellipsometry [79, 80]. Especially, Xie et al. reported on a theoretical model study of the optical conductivity of t_2g 2DEGs formed at perovskite oxide surfaces and interfaces. They find out that by measuring the Drude weight of the t_2g 2DEG, it is possible to provide an estimate of the total 2D carrier density. They also show that in 2DEGs with a large 2D carrier density, a plasmon-like collective mode, resulting from Coulomb coupling induces in-phase oscillation of a large number of intersubband transitions 6.1.

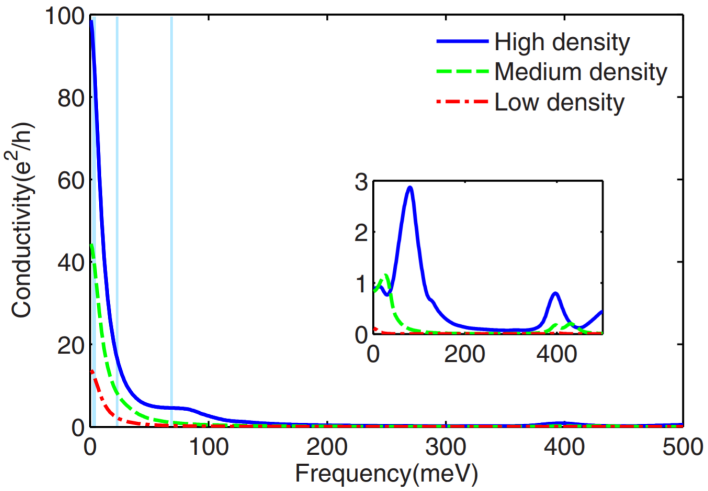

FIGURE 6.1. From Xie et Al [80] : In-plane optical conductivity of a $SrTiO_3$ 2DEG in e^2/h units for light polarized in the plane of the t_{2_g} 2DEG at high density (5.9×10^{-14} cm^{-2}) medium (2×10^{-14} cm^{-2}), and low (2.3×10^{-13} cm^{-2}) carrier densities 2DEG with strong atomic spin-orbit coupling with strength Δ_{SO} = 400 meV. The inset plots the intersubband part only. The disorder-broadening η has been set to 10 meV.

Preliminary results

We show the preliminary results of the ellipsometry results of Cu/Bi_2O_3 shown in figure 6.2. We can see a good resemblance between the theoretical prediction 6.1 and red curve of figure 6.2 (a) regarding decreasing as figure 6.2 (a) shows the Drude contribution on the dielectric component through the photon energy. Moreover, the more detailed analysis comparable to the inset of 6.1 inset is shown figure 6.2 (b) and shows the possible spin-orbit coupling contribution on the dielectric component through the photon energy. These results may be a direct confirmation of the existence of a 2DEG in the Cu/Bi_2O_3 but further analysis with control samples are necessary.

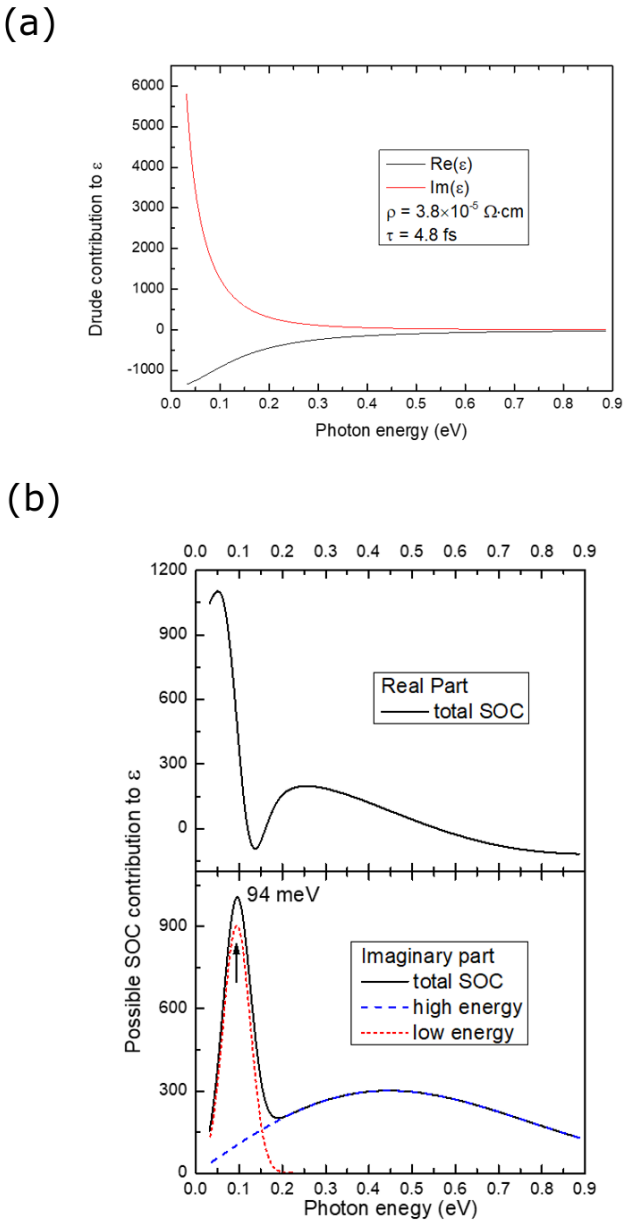

FIGURE 6.2. Ellipsometry measurement of Cu/Bi_2O_3. (a) shows the Drude contribution on the dielectric component through the photon energy. (b) shows the possible spin-orbit coupling contribution on the dielectric component through the photon energy.

6.2.2 Understanding the mechanism at the interface

The other way to understand what is happening at the interface is to use first principle calculation. At the interface, it may be possible to observe the hybridization of states between Cu and Bi_2O_3 that would confirm the assumption made in Chapter 4 and clarify the origin of the signal of the photovoltage of 1.96eV.

Preliminary results

In collaboration with Ishii group from Kanazawa University, we show that from first principle calculation that at the interface, it is possible to observe the hybridization of states between Cu and Bi_2O_3. This hybridization is the resultant of the charge transfer mechanism. A sketched of the calculated charge density of the electronic state of the Cu(111)/α-Bi_2O_3 interface is shown 6.3 (b); where blue, red and purple spheres are Cu, O and Bi atoms, respectively; yellow clouds show the hybridization of Cu-O-Bi states. Moreover, analysis of the calculated electronic structure in between 1.84 eV and 2 eV on top of the Fermi level displays a Rashba spin splitting in the range of 1.98-1.99 eV is shown in figure 6.3 (c). This Rashba splitting is the consequence of hybridization and broken spatial inversion symmetry at our interface, which facilitates our helicity dependent photovoltaic conversion.

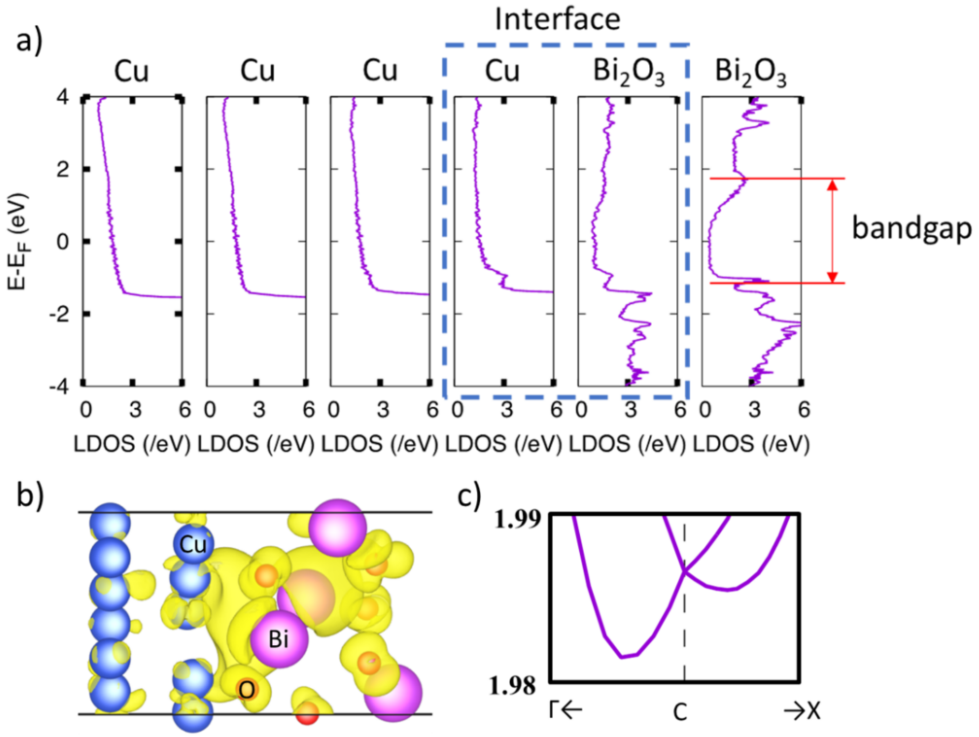

FIGURE 6.3. First-principles analysis of the Cu/Bi_2O_3 interface. (a) The layer-projected density of states (LDOS) at the Cu/Bi_2O_3 interface (dashed line zone) and its vicinity. The LDOS of Bi_2O_3 is from every two bismuth and three oxygen atoms in order of proximity to the interfacial Cu layer. (b) Schematic representation of the charge density of the electronic states of the Cu(111)/ α-Bi_2O_3 interface. Blue, red and purple spheres are Cu, O and Bi atoms, respectively; yellow clouds show the hybridization of Cu-O-Bi states.(c) Rashba spin splitting in the range of 1.98-1.99 eV around the C-point in the Brillouin zone, where the origin in energy is set to be the Fermi level and there are special points: Γ (0, 0, 0); C (1/2, 1/2, 0); X (1/2, 0, 0)

BIBLIOGRAPHY

[1] M. N. Baibich, J. M. Broto, A. Fert, F. N. Van Dau, F. Petroff, P. Etienne, G. Creuzet, A. Friederich, and J. Chazelas, "Giant Magnetoresistance of (001)Fe/ (001)Cr magnetic superlattices," *Phys. Rev. Lett.*, vol. 61, pp. 2472–2475, Nov 1988.

[2] G. Binasch, P. Grünberg, F. Saurenbach, and W. Zinn, "Enhanced magnetoresistance in layered magnetic structures with antiferromagnetic interlayer exchange," *Phys. Rev. B*, vol. 39, pp. 4828–4830, Mar 1989.

[3] "Millennium technology prize for Stuart Parkin in 2014." https://taf.fi/millennium-technology-prize/winner-2014/.
Accessed: 2018-05-29.

[4] Y. Otani, M. Shiraishi, A. Oiwa, E. Saitoh, and S. Murakami, "Spin conversion on the nanoscale," *Nature Physics*, vol. 13, 07 2017.

[5] A. Manchon, H. C. Koo, J. Nitta, S. M. Frolov, and R. A. Duine, "New perspectives for Rashba spin-orbit coupling," *Nature Materials*, vol. 14, pp. 871 EP –, Aug 2015.

[6] Y. K. Kato, R. C. Myers, A. C. Gossard, and D. D. Awschalom, "Observation of the spin Hall effect in semiconductors," *Science*, vol. 306, no. 5703, pp. 1910–1913, 2004.

[7] E. Saitoh, M. Ueda, H. Miyajima, and G. Tatara, "Conversion of spin current into charge current at room temperature: Inverse spin-Hall effect," *Applied Physics Letters*, vol. 88, no. 18, p. 182509, 2006.

[8] Y. Tserkovnyak, A. Brataas, and G. E. W. Bauer, "Spin pumping and magnetization dynamics in metallic multilayers," *Phys. Rev. B*, vol. 66, p. 224403, Dec 2002.

[9] Y. Tserkovnyak, A. Brataas, and G. E. W. Bauer, "Enhanced gilbert damping in thin ferromagnetic films," *Phys. Rev. Lett.*, vol. 88, p. 117601, Feb 2002.

[10] T. Kimura, Y. Otani, T. Sato, S. Takahashi, and S. Maekawa, "Room-temperature reversible spin Hall effect," *Phys. Rev. Lett.*, vol. 98, p. 156601, Apr 2007.

[11] M. Morota, Y. Niimi, K. Ohnishi, D. H. Wei, T. Tanaka, H. Kontani, T. Kimura, and Y. Otani, "Indication of intrinsic spin Hall effect in 4d and 5d transition metals," *Phys. Rev. B*, vol. 83, p. 174405, May 2011.

[12] Y. Niimi, M. Morota, D. H. Wei, C. Deranlot, M. Basletic, A. Hamzic, A. Fert, and Y. Otani, "Extrinsic spin Hall effect induced by iridium impurities in copper," *Phys. Rev. Lett.*, vol. 106, p. 126601, Mar 2011.

[13] Y. Niimi, Y. Kawanishi, D. H. Wei, C. Deranlot, H. X. Yang, M. Chshiev, T. Valet, A. Fert, and Y. Otani, "Giant spin Hall effect induced by skew scattering from bismuth impurities inside thin film cubi alloys," *Phys. Rev. Lett.*, vol. 109, p. 156602, Oct 2012.

[14] W. Yan, E. Sagasta, M. Ribeiro, Y. Niimi, L. E. Hueso, and F. Casanova, "Large room temperature spin-to-charge conversion signals in a few-layer graphene/pt lateral heterostructure," *Nature Communications*, vol. 8, no. 1, p. 661, 2017.

[15] J. Tian, I. Miotkowski, S. Hong, and Y. P. Chen, "Electrical injection and detection of spin-polarized currents in topological insulator Bi(2)Te(2)Se," *Sci. Rep*, vol. 5, p. 14293, Sep 2015.

[16] K. Ando, M. Morikawa, T. Trypiniotis, Y. Fujikawa, C. Barnes, and E. Saitoh, "Direct conversion of light-polarization information into electric voltage using photoinduced inverse spin-Hall effect in Pt/GaAs hybrid structure: Spin photodetector," *Journal of Applied Physics*, vol. 107, pp. 113902 – 113902, 07 2010.

[17] S. Khamari, S. Porwal, V. Dixit, and T. Sharma, "Temperature dependence of the photo-induced inverse spin Hall effect in Au/InP hybrid structures," *Applied Physics Letters*, vol. 104, pp. 042102–042102, 01 2014.

[18] F. Bottegoni, A. Ferrari, S. Cecchi, M. Finazzi, F. Ciccacci, and G. Isella, "Photoinduced inverse spin Hall effect in Pt/Ge(001) at room temperature," *Applied Physics Letters*, vol. 102, 02 2013.

[19] F. Bottegoni, C. Zucchetti, F. Ciccacci, M. Finazzi, and G. Isella, "Optical generation of pure spin currents at the indirect gap of bulk Si," *Applied Physics Letters*, vol. 110, p. 042403, 01 2017.

[20] S. Datta and B. Das, "Electronic analog of the electro-optic modulator," *Applied Physics Letters*, vol. 56, no. 7, pp. 665–667, 1990.

[21] J. Nitta, T. Akazaki, H. Takayanagi, and T. Enoki, "Gate control of spin-orbit interaction in an inverted $In_{0.53}Ga_{0.47}As/In_{0.52}Al_{0.48}As$ heterostructure," *Phys. Rev. Lett.*, vol. 78, pp. 1335–1338, Feb 1997.

[22] S. D. Ganichev, V. V. Bel'kov, L. E. Golub, E. L. Ivchenko, P. Schneider, S. Giglberger, J. Eroms, J. De Boeck, G. Borghs, W. Wegscheider, D. Weiss, and W. Prettl, "Experimental separation of Rashba and Dresselhaus spin splittings in semiconductor quantum wells," *Phys. Rev. Lett.*, vol. 92, p. 256601, Jun 2004.

[23] J. C. Rojas Sánchez, L. Vila, G. Desfonds, S. Gambarelli, J. P Attané, J. De Teresa, C. Magén, and A. Fert, "Spin-to-charge conversion using Rashba coupling at the interface between non-magnetic materials," *Nature communications*, vol. 4, p. 2944, 12 2013.

[24] J.-C. Rojas-Sánchez, S. Oyarzún, Y. Fu, A. Marty, C. Vergnaud, S. Gambarelli, L. Vila, M. Jamet, Y. Ohtsubo, A. Taleb-Ibrahimi, P. Le Fèvre, F. Bertran, N. Reyren, J.-M. George, and A. Fert, "Spin to charge conversion at room temperature by spin pumping into a new type of topological insulator: α-sn films," *Phys. Rev. Lett.*, vol. 116, p. 096602, Mar 2016.

[25] S. Karube, H. Idzuchi, K. Kondou, Y. Fukuma, and Y. Otani, "Spin relaxation characteristics in Ag nanowire covered with various oxides," *Applied Physics Letters*, vol. 107, no. 12, p. 122406, 2015.

[26] L. Leontie, M. Caraman, M. Alexe, and C. Harnagea, "Structural and optical characteristics of bismuth oxide thin films," *Surface Science*, vol. 507-510, pp. 480 – 485, 2002.

[27] K. Braun, "Studien über erd-magnetische messungen," *Annalen der Physik*, 1874.

[28] H. Luth, *Solid Surfaces, Interfaces and Thin Films*.
Springer International Publishing, 6 ed., 2015.

[29] J. Bardeen, "Surface states and rectification at a metal semi-conductor contact," *Phys. Rev.*, vol. 71, pp. 717–727, May 1947.

[30] W. Mönch, "Branch-point energies and the band-structure lineup at schottky contacts and heterostrucures," *Journal of Applied Physics*, vol. 109, no. 11, p. 113724, 2011.

[31] D. K. Schroder, "Surface voltage and surface photovoltage: history, theory and applications," *Measurement Science and Technology*, vol. 12, no. 3, p. R16, 2001.

[32] R. E. I. Bychkov Yu. A., "Properties of a 2d electron gas with lifted spectral degeneracy," *JETP Letters*, vol. 39, no. 2, p. 78, 1984.

[33] G. Bihlmayer, S. Blügel, and E. V. Chulkov, "Enhanced Rashba spin-orbit splitting in Bi/Ag(111) and Pb/Ag surface alloys from first principles," *Physical Review B*, vol. 75, no. 19, p. 195414, 2007.

[34] I. Gierz, B. Stadtmüller, J. Vuorinen, M. Lindroos, F. Meier, J. H. Dil, K. Kern, and C. R. Ast, "Structural influence on the Rashba-type spin splitting in surface alloys," *Physical Review B*, vol. 81, no. 24, p. 245430, 2010.

[35] V. M. Edelstein, "Spin polarization of conduction electrons induced by electric current in two-dimensional asymmetric electron systems," *Solid State Communications*, vol. 73, no. 3, pp. 233–235, 1990.

[36] K. K. Shutaro Karube and Y. Otani, "Experimental observation of spin-to-charge current conversion at non-magnetic metal/bi2o3 interfaces," *Applied Physics Express*, vol. 9, no. 3, p. 033001, 2016.

[37] R. W. Wood, "On a remarkable case of uneven distribution of light in a diffraction grating spectrum," *Proceedings of the Physical Society of London*, vol. 18, no. 1, p. 269, 1902.

[38] U. Fano, "The theory of anomalous diffraction gratings and of quasi-stationary waves on metallic surfaces (sommerfeld's waves)," *J. Opt. Soc. Am.*, vol. 31, pp. 213–222, Mar 1941.

[39] R. H. Ritchie, "Plasma losses by fast electrons in thin films," *Phys. Rev.*, vol. 106, pp. 874–881, Jun 1957.

[40] K. Catchpole and A. Polman, "Plasmonic solar cells," *Opt. Express*, vol. 16, pp. 21793–21800, Dec 2008.

[41] M. Fox, "Optical properties of solids," *American Journal of Physics*, vol. 70, no. 12, pp. 1269–1270, 2002.

[42] R. Carey and B. W. J. Thomas, "The theory of the voigt effect in ferromagnetic materials," *Journal of Physics D: Applied Physics*, vol. 7, no. 17, p. 2362, 1974.

[43] J. M. Florczak and E. D. Dahlberg, "Detecting two magnetization components by the magneto-optical kerr effect," *Journal of Applied Physics*, vol. 67, no. 12, pp. 7520–7525, 1990.

[44] D. A. Allwood, P. R. Seem, S. Basu, P. W. Fry, U. J. Gibson, and R. P. Cowburn, "Over 40% transverse kerr effect from $Ni_{80}Fe_{20}$," *Applied Physics Letters*, vol. 92, no. 7, p. 072503, 2008.

[45] G. Binnig and H. Rohrer, "Scanning tunneling microscopy—from birth to adolescence," *Rev. Mod. Phys.*, vol. 59, pp. 615–625, Jul 1987.

[46] L. H. G. Addison H. White, "The rate of oxidation of copper at room temperature," *Journal of The Electrochemical Society*, vol. 81, pp. 305–319, 1942.

[47] Z. Yang, C. Liu, Y. Gao, J. Wang, and W. Yang, "Influence of surface roughness on surface plasmon resonance phenomenon of gold film," *Chin. Opt. Lett.*, vol. 14, p. 042401, Apr 2016.

[48] J. Tauc, R. Grigorovici, and A. Vancu, "Optical properties and electronic structure of amorphous germanium," *physica status solidi (b)*, vol. 15, no. 2, pp. 627–637.

[49] O. M. J. vant Erve, A. T. Hanbicki, K. M. McCreary, C. H. Li, and B. T. Jonker, "Optical detection of spin Hall effect in metals," *Applied Physics Letters*, vol. 104, no. 17, p. 172402, 2014.

[50] C. Stamm, C. Murer, M. Berritta, J. Feng, M. Gabureac, P. M. Oppeneer, and P. Gambardella, "Magneto-optical detection of the spin Hall effect in Pt and W thin films," *Phys. Rev. Lett.*, vol. 119, p. 087203, Aug 2017.

[51] Y. Su, H. Wang, J. Li, C. Tian, R. Wu, X. Jin, and Y. R. Shen, "Absence of detectable moke signals from spin Hall effect in metals," *Applied Physics Letters*, vol. 110, no. 4, p. 042401, 2017.

[52] P. Riego, S. Vélez, J. M. Gomez-Perez, J. A. Arregi, L. E. Hueso, F. Casanova, and A. Berger, "Absence of detectable current-induced magneto-optical kerr effects in pt, ta, and w," *Applied Physics Letters*, vol. 109, no. 17, p. 172402, 2016.

[53] H. Tsai, S. Karube, K. Kondou, N. Yamaguchi, F. Ishii, and Y. Otani, "Clear variation of spin splitting by changing electron distribution at non-magnetic metal/bi2o3 interfaces," *Scientific Reports*, vol. 8, no. 1, p. 5564, 2018.

[54] J. Kim, Y.-T. Chen, S. Karube, S. Takahashi, K. Kondou, G. Tatara, and Y. Otani, "Evaluation of bulk-interface contributions to edelstein magnetoresistance at metal/oxide interfaces," *Phys. Rev. B*, vol. 96, p. 140409, Oct 2017.

[55] A. Yagmur, S. Karube, K. Uchida, K. Kondou, R. Iguchi, T. Kikkawa, Y. Otani, and E. Saitoh, "Spin-current-driven thermoelectric generation based on interfacial spin-orbit coupling," *Applied Physics Letters*, vol. 108, no. 24, p. 242409, 2016.

[56] P. Gambardella and I. M. Miron, "Current-induced spin–orbit torques," *Philosophical Transactions of the Royal Society of London A: Mathematical, Physical and Engineering Sciences*, vol. 369, no. 1948, pp. 3175–3197, 2011.

[57] A. Barman, T. Kimura, Y. Otani, Y. Fukuma, K. Akahane, and S. Meguro, "Bench-top time-resolved magneto-optical kerr magnetometer," *Review of Scientific Instruments*, vol. 79, no. 12, p. 123905, 2008.

[58] X. Feng, Y. Li, Y. Qin, Y. Xiao, H. Yang, and Q. Gong, "Dependence of femtosecond time-resolved magneto-optical kerr rotation on the direction of polarization of the probe beam," *Science China Physics, Mechanics and Astronomy*, vol. 54, pp. 1411–1415, Aug 2011.

[59] E. Oblak, P. Riego, L. Fallarino, A. M. de Guerenu, F. Arizti, and A. Berger, "Ultrasensitive transverse magneto-optical kerr effect measurements by means of effective polarization change detection," *Journal of Physics D: Applied Physics*, vol. 50, no. 23, p. 23LT01, 2017.

[60] J. Hu, D. W. Shen, and D. L. Feng, "Spin polarization and dichroism effects induced by an electric field," *Phys. Rev. B*, vol. 73, p. 085325, Feb 2006.

[61] J. Shibata, A. Takeuchi, H. Kohno, and G. Tatara, "Theory of anomalous optical properties of bulk Rashba conductor," *Journal of the Physical Society of Japan*, vol. 85, no. 3, p. 033701, 2016.

[62] H. Bentmann, T. Kuzumaki, G. Bihlmayer, S. Blügel, E. V. Chulkov, F. Reinert, and K. Sakamoto, "Spin orientation and sign of the Rashba splitting in Bi/Cu(111)," *Phys. Rev. B*, vol. 84, p. 115426, Sep 2011.

[63] T. Kimura, J. Hamrle, and Y. Otani, "Estimation of spin-diffusion length from the magnitude of spin-current absorption: Multiterminal ferromagnetic/nonferromagnetic hybrid structures," *Phys. Rev. B*, vol. 72, p. 014461, Jul 2005.

[64] P. B. Johnson and R. W. Christy, "Optical constants of the noble metals," *Phys. Rev. B*, vol. 6, pp. 4370–4379, Dec 1972.

[65] D. Ellsworth, L. Lu, J. Lan, H. Chang, P. Li, Z. Wang, J. Hu, B. Johnson, Y. Bian, J. Xiao, R. Wu, and M. Wu, "Photo-spin-voltaic effect," *Nature Physics*, vol. 12, pp. 861 EP –, Apr 2016.

[66] W. Weber, S. D. Ganichev, S. N. Danilov, D. Weiss, W. Prettl, Z. D. Kvon, V. V. Belkov, L. E. Golub, H.-I. Cho, and J.-H. Lee, "Demonstration of Rashba spin splitting in gan-based heterostructures," *Applied Physics Letters*, vol. 87, no. 26, p. 262106, 2005.

[67] S. Condurache-Bota, G. I. Rusu, N. Tigau, and L. Leontie, "Important physical parameters of bi2o3 thin films found by applying several models for optical data," *Crystal Research and Technology*, vol. 45, no. 5, pp. 503–511, 2010.

[68] V. G. Kravets, R. Jalil, Y.-J. Kim, D. Ansell, D. E. Aznakayeva, B. Thackray, L. Britnell, B. D. Belle, F. Withers, I. P. Radko, Z. Han, S. I. Bozhevolnyi, K. S. Novoselov, A. K. Geim, and A. N. Grigorenko, "Graphene-protected copper and silver plasmonics," *Scientific Reports*, vol. 4, pp. 5517–, Jul 2014.

[69] S. V. Zhukovsky, V. E. Babicheva, A. B. Evlyukhin, I. E. Protsenko, A. V. Lavrinenko, and A. V. Uskov, "Giant photogalvanic effect in noncentrosymmetric plasmonic nanoparticles," *Phys. Rev. X*, vol. 4, p. 031038, Sep 2014.

[70] C. Clavero, "Plasmon-induced hot-electron generation at nanoparticle/metal-oxide interfaces for photovoltaic and photocatalytic devices," *Nature Photonics*, vol. 8, pp. 95 –, Jan 2014.

[71] M. Kiguchi, R. Arita, G. Yoshikawa, Y. Tanida, M. Katayama, K. Saiki, A. Koma, and H. Aoki, "Metal-induced gap states at well defined alkali-halide/metal interfaces," *Phys. Rev. Lett.*, vol. 90, p. 196803, May 2003.

[72] N. Seriani, C. Pinilla, and Y. Crespo, "Presence of gap states at cu/tio2 anatase surfaces: Consequences for the photocatalytic activity," *The Journal of Physical Chemistry C*, vol. 119, no. 12, pp. 6696–6702, 2015.

[73] D. A. Muller, D. A. Shashkov, R. Benedek, L. H. Yang, J. Silcox, and D. N. Seidman, "Atomic scale observations of metal-induced gap states at 222 mgo/cu interfaces," *Phys. Rev. Lett.*, vol. 80, pp. 4741–4744, May 1998.

[74] T. Nishimura, K. Kita, and A. Toriumi, "Evidence for strong fermi-level pinning due to metal-induced gap states at metal/germanium interface," *Applied Physics Letters*, vol. 91, no. 12, p. 123123, 2007.

[75] C. Gong, L. Colombo, R. M. Wallace, and K. Cho, "The unusual mechanism of partial fermi level pinning at metal-mos2 interfaces," *Nano Letters*, vol. 14, pp. 1714–1720, Apr 2014.

[76] T. Tatsuma, H. Nishi, and T. Ishida, "Plasmon-induced charge separation: chemistry and wide applications," *Chem. Sci.*, vol. 8, pp. 3325–3337, 2017.

[77] A. Furube and S. Hashimoto, "Insight into plasmonic hot-electron transfer and plasmon molecular drive: new dimensions in energy conversion and nanofabrication," *Npg Asia Materials*, vol. 9, pp. 454 –, Dec 2017.

[78] T. Hatano, T. Ishihara, S. G. Tikhodeev, and N. A. Gippius, "Transverse photovoltage induced by circularly polarized light," *Phys. Rev. Lett.*, vol. 103, p. 103906, Sep 2009.

[79] G. Khalsa, B. Lee, and A. H. MacDonald, "Theory of t_{2g} electron-gas Rashba interactions," *Phys. Rev. B*, vol. 88, p. 041302, Jul 2013.

[80] M. Xie, G. Khalsa, and A. H. MacDonald, "Optical conductivity of the t_{2g} two-dimensional electron gas," *Phys. Rev. B*, vol. 89, p. 245417, Jun 2014.